



THE UNIVERSITY *of* EDINBURGH

Edinburgh Research Explorer

Coupled evolution of temperature and carbonate chemistry during the Paleocene–Eocene; new trace element records from the low latitude Indian Ocean

Citation for published version:

Barnet, JSK, Harper, DT, LeVay, LJ, Edgar, KM, Henehan, MJ, Babila, TL, Ullmann, CV, Leng, MJ, Kroon, D, Zachos, JC & Littler, K 2020, 'Coupled evolution of temperature and carbonate chemistry during the Paleocene–Eocene; new trace element records from the low latitude Indian Ocean', *Earth and Planetary Science Letters*, vol. 545, pp. 116414. <https://doi.org/10.1016/j.epsl.2020.116414>

Digital Object Identifier (DOI):

[10.1016/j.epsl.2020.116414](https://doi.org/10.1016/j.epsl.2020.116414)

Link:

[Link to publication record in Edinburgh Research Explorer](#)

Document Version:

Publisher's PDF, also known as Version of record

Published In:

Earth and Planetary Science Letters

General rights

Copyright for the publications made accessible via the Edinburgh Research Explorer is retained by the author(s) and / or other copyright owners and it is a condition of accessing these publications that users recognise and abide by the legal requirements associated with these rights.

Take down policy

The University of Edinburgh has made every reasonable effort to ensure that Edinburgh Research Explorer content complies with UK legislation. If you believe that the public display of this file breaches copyright please contact openaccess@ed.ac.uk providing details, and we will remove access to the work immediately and investigate your claim.





Coupled evolution of temperature and carbonate chemistry during the Paleocene–Eocene; new trace element records from the low latitude Indian Ocean

James S.K. Barnet^{a,*}, Dustin T. Harper^{b,c}, Leah J. LeVay^d, Kirsty M. Edgar^e, Michael J. Henehan^f, Tali L. Babila^{b,g}, Clemens V. Ullmann^a, Melanie J. Leng^{h,i}, Dick Kroon^j, James C. Zachos^b, Kate Littler^a

^a Camborne School of Mines and Environment and Sustainability Institute, University of Exeter, Penryn Campus, Cornwall, UK

^b Department of Earth and Planetary Sciences, University of California Santa Cruz, Santa Cruz, CA, USA

^c Department of Geology, The University of Kansas, Lawrence, KS 66045, USA

^d International Ocean Discovery Program, Texas A&M University, College Station, TX, USA

^e School of Geography, Earth and Environmental Sciences, University of Birmingham, Birmingham, UK

^f GFZ German Research Centre for Geosciences, Section Earth Surface Geochemistry, Telegrafenberg, 14473 Potsdam, Germany

^g Ocean and Earth Science, National Oceanography Centre Southampton, University of Southampton, Southampton, UK

^h NERC Isotope Geosciences Facility, British Geological Survey, Nottingham, NG12 5GG, UK

ⁱ Centre for Environmental Geochemistry, School of Biosciences, Sutton Bonington Campus, University of Nottingham, Loughborough, UK

^j School of GeoSciences, University of Edinburgh, Edinburgh, UK

ARTICLE INFO

Article history:

Received 22 January 2020

Received in revised form 3 June 2020

Accepted 8 June 2020

Available online xxxx

Editor: L. Robinson

Keywords:

trace elements

paleoclimate

paleoceanography

Paleogene

Paleocene–Eocene Thermal Maximum

Indian Ocean

ABSTRACT

The early Paleogene represents the most recent interval in Earth's history characterized by global greenhouse warmth on multi-million year timescales, yet our understanding of long-term climate and carbon cycle evolution in the low latitudes, and in particular the Indian Ocean, remains very poorly constrained. Here we present the first long-term sub-eccentricity-resolution stable isotope ($\delta^{13}\text{C}$ and $\delta^{18}\text{O}$) and trace element (Mg/Ca and B/Ca) records spanning the late Paleocene–early Eocene (~58–53 Ma) across a surface–deep hydrographic reconstruction of the northern Indian Ocean, resolving late Paleocene 405-kyr paced cyclicity and a portion of the PETM recovery. Our new records reveal a long-term warming of ~4–5 °C at all depths in the water column, with absolute surface ocean temperatures and magnitudes of warming comparable to the low latitude Pacific. As a result of warming, we observe a long-term increase in $\delta^{18}\text{O}_{\text{sw}}$ of the mixed layer, implying an increase in net evaporation. We also observe a collapse in the temperature gradient between mixed layer- and thermocline-dwelling species from ~57–54 Ma, potentially due to either the development of a more homogeneous water column with a thicker mixed layer, or depth migration of the *Morozovella* in response to warming. Synchronous warming at both low and high latitudes, along with decreasing B/Ca ratios in planktic foraminifera indicating a decrease in ocean pH and/or increasing dissolved inorganic carbon, suggest that global climate was forced by rising atmospheric CO_2 concentrations during this time.

© 2020 The Author(s). Published by Elsevier B.V. This is an open access article under the CC BY license (<http://creativecommons.org/licenses/by/4.0/>).

1. Introduction

The early Paleogene has emerged as the subject of much interest as it represents the most recent interval in Earth's history characterized by sustained global greenhouse warmth, and was punctuated by transient warming events termed “hyperther-

mals”, which may represent the closest analogues for future anthropogenic climate change. Early paleoclimatic studies across this enigmatic time interval focused on the generation of long-term low-resolution stable oxygen isotope ($\delta^{18}\text{O}$) records from a suite of planktic and benthic foraminifera species, from which surface and deep ocean temperatures could be reconstructed, respectively, assuming an ice-free world (e.g., Shackleton and Kennett, 1975; Stott et al., 1990; Zachos et al., 1992, 1994; Bralower et al., 1995). While painting a picture of the broad longer term paleoclimatic and paleoenvironmental changes at both the low and high latitudes, identifying major hyperthermals such as the Paleocene–

* Corresponding author at: School of Earth and Environmental Sciences, University of St Andrews, St Andrews, Scotland, UK.

E-mail address: jsb24@st-andrews.ac.uk (J.S.K. Barnet).

Eocene Thermal Maximum (PETM) and Eocene Thermal Maximum 2 (ETM-2), and providing a first attempt to quantify absolute temperatures and equator-pole temperature gradients, the resolution of these early studies was generally insufficient to elucidate background orbital cyclicity and pacing of the major climatic events. In addition, planktic foraminiferal $\delta^{18}\text{O}$ can be heavily biased by factors other than temperature change in an ice-free world, including local changes in net precipitation or evaporation from the surface ocean, and primary foraminiferal $\delta^{18}\text{O}$ signatures can be overprinted by significant diagenetic recrystallization. Therefore, an independent temperature proxy such as planktic Mg/Ca is required in order to better constrain absolute temperatures and the magnitude of change within the surface ocean.

Paired foraminiferal Mg/Ca and B/Ca data have emerged as promising proxies for unraveling the coupled temperature and carbonate chemistry [related to pH and dissolved inorganic carbon (DIC)] characteristics of the portion of the water column inhabited by foraminifera (e.g., Penman et al., 2014; Babila et al., 2016). These proxies have been extensively and successfully applied to understand temperature and carbonate chemistry changes during Plio-Pleistocene glacial-interglacial cycles using extant planktic foraminiferal species, where the species-specific relationship between trace element data and seawater characteristics has been constrained by laboratory culture experiments (e.g., Evans et al., 2016a, 2016b; Haynes et al., 2019), sediment trap studies (e.g., Anand et al., 2003; Gray et al., 2018), and core-top analyses (e.g., Brown et al., 2011; Stainbank et al., 2019). However, the use of these proxies further back into geological time is complicated by the lack of extant planktic foraminiferal species, and, until recently, the poorly constrained evolution of the pH and chemical composition of the oceans, e.g., seawater Mg/Ca ratio ($\text{Mg}/\text{Ca}_{\text{sw}}$) and B concentration $[\text{B}]_{\text{sw}}$. In the past few years, significant advances have been made in our understanding of the evolution of these variables during the Cenozoic and how foraminiferal Mg/Ca and B/Ca proxy sensitivities would have responded to them (e.g., Lemarchand et al., 2002; Allen et al., 2011, 2012; Evans et al., 2016a, 2016b, 2018; Babila et al., 2018; Haynes et al., 2019; Zeebe and Tyrrell, 2019), extending the utility of these geochemical proxies back into the greenhouse world of the early Paleogene.

To date, applications of trace element proxies to Paleogene oceans have been predominantly focused on the hyperthermal events, such as the PETM (e.g., Zachos et al., 2003; Tripati and Elderfield, 2004; Penman et al., 2014; Babila et al., 2016, 2018) and ETM-2 (Harper et al., 2018), with a smaller number of low-resolution longer-term studies (e.g., Lear et al., 2000, 2015; Tripati et al., 2003; Dutton et al., 2005). However, without placing hyperthermal events into the context of long-term change in global climate, it is challenging to understand how suitable they are as analogues for anthropogenic climate change. Furthermore, previous Paleogene studies have mainly focused on sites in or bordering the Atlantic and Pacific Oceans, with a paucity of high-resolution long-term geochemical records from the Indian Ocean, hampering our understanding of temperature and carbonate chemistry evolution in this ocean basin. Our understanding of the broader low latitude response to greenhouse warming and ability to quantify equator-pole temperature gradients have also been hindered by the paucity of early Paleogene marine records that yield suitably well-preserved foraminifera for the generation of reliable trace element data from the low latitude and equatorial regions. Low latitude sites are the most susceptible to diagenetic bias (e.g., Pearson and Wade, 2009), but are critical for constraining low latitude sensitivity to greenhouse gas forcing.

This study focuses on creating sub-eccentricity-resolution trace element and stable isotope records spanning the late Paleocene-early Eocene (~58–53 Ma) from a new splice developed between International Ocean Discovery Program (IODP) Site U1443 and

Ocean Drilling Program (ODP) Site 758 in the low latitude Indian Ocean. We generated coupled Mg/Ca and B/Ca data from well-preserved mixed layer, thermocline-dwelling and benthic foraminifera, along with stable isotope ($\delta^{13}\text{C}$ and $\delta^{18}\text{O}$) data from mixed layer-dwelling planktic foraminifera, to reconstruct temperature and carbonate chemistry changes through the water column in the northern Indian Ocean spanning the late Paleocene-early Eocene.

2. Materials and methods

This study used samples recovered from a splice between IODP Hole U1443A (5°23′0.59″N, 90°21′42.6″E; 2,929 m water depth) and ODP Hole 758A (5°23′3.12″N, 90°21′40.32″E; 2,924 m water depth), drilled ~100 m apart on the shallow crest of the Ninetyeast Ridge (paleolatitude ~29°S; Shipboard Scientific Party, 1989; Clemens et al., 2016; Fig. 1). Although Paleocene-Eocene sediment cores characterized by higher sedimentation rates and greater stratigraphic completeness have been recovered from the Atlantic, Pacific and Southern oceans, IODP Site U1443 and ODP Site 758 were specifically chosen to shed new light on the paleoclimatic and paleoceanographic evolution of the poorly studied low latitude Indian Ocean, to identify if the temperature and carbonate chemistry trends observed in contemporaneous records from the low latitude Atlantic and Pacific oceans are indeed global in scale. The Paleogene strata were drilled using the Extended Core Barrel (XCB) system at both sites, resulting in a series of core biscuits surrounded by drilling slurry. Each easily identifiable core biscuit was sampled at ~1–20 cm resolution, with bulk sediment carbon isotope ($\delta^{13}\text{C}_{\text{bulk}}$) data generated for each sample and planktic stable isotope ($\delta^{13}\text{C}_{\text{planktic}}$ and $\delta^{18}\text{O}_{\text{planktic}}$) and trace element (Mg/Ca and B/Ca) data generated at ~5–60 cm resolution (increased to ~3–4 cm resolution across the PETM interval). This sampling strategy enables a temporal resolution for the planktic trace element records of typically ~10–60 kyr in the late Paleocene and ~30–100 kyr in the early Eocene portions of the record based on our age model (described below). The benthic trace element records were generated at a comparable resolution to the planktic trace element records, with the exception of the late Paleocene portion of the benthic Mg/Ca record, which was generated at a lower resolution of ~100–500 kyr due to the scarcity of *Oridorsalis umbonatus* within the late Paleocene cores from these sites. The shallow paleo-depth of these sites (~1,500 m; Clemens et al., 2016), well above the early Paleogene calcite compensation depth (CCD; ~4,000 m; Slotnick et al., 2015), protected foraminiferal specimens from significant dissolution and resulted in generally good preservation, with only relatively minor recrystallization of test walls evident under SEM (see Supplementary Information Section 7.0; Figs. S3–S5). The absence of a negative correlation between Sr/Ca and Mg/Ca ratios within the sample set, along with the majority of samples having Sr/Ca values >1 mmol/mol (Supplementary Fig. S6), suggest that the trace element records discussed here are not significantly biased by diagenesis (Kozdon et al., 2013; Edgar et al., 2015). It should also be noted that preservation of these planktic foraminifera is generally better than samples from other low latitude Paleocene-Eocene sites where contemporaneous trace element records have been generated, such as ODP Site 1209 (e.g., Zachos et al., 2003) and ODP Site 865 (e.g., Edgar et al., 2015) in the equatorial Pacific, which are characterized by more significant recrystallization.

The age model and splice between the sites was generated using $\delta^{13}\text{C}_{\text{bulk}}$ stratigraphy, integrated with high-resolution calcareous nannofossil and lower resolution planktic foraminiferal biostratigraphy (Fig. 2; Tables 1–2). Ages for the chemostratigraphic and biostratigraphic events were taken from the age model of Barnet et al. (2019), orbitally tuned to the La2010b orbital solu-

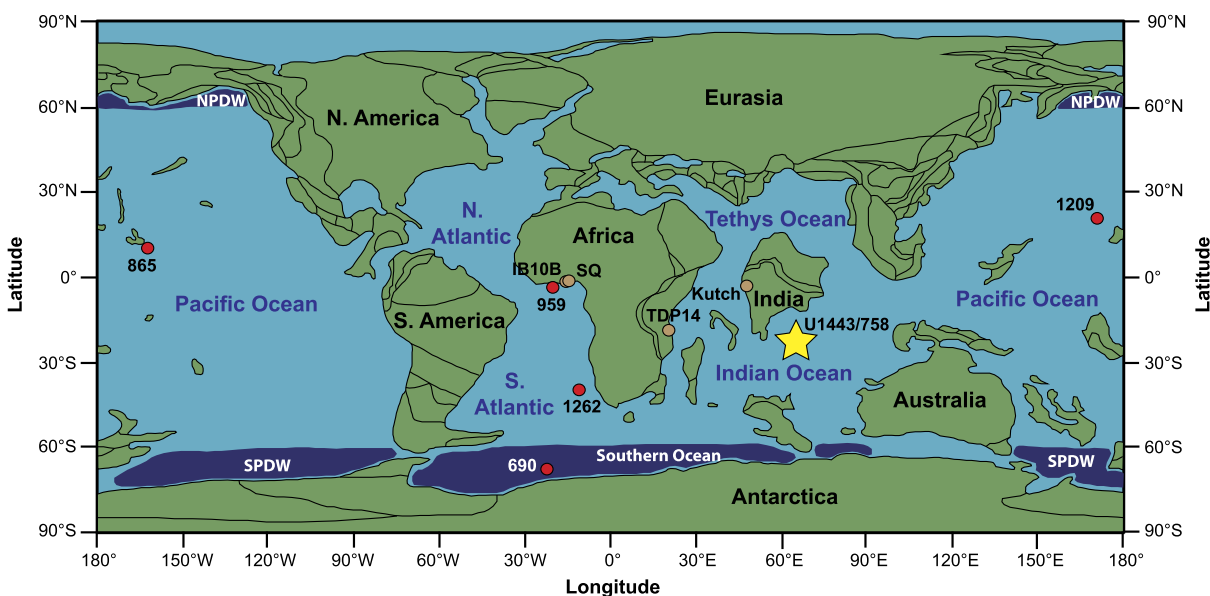


Fig. 1. Paleogeographic reconstruction for ~56 Ma [the Paleocene-Eocene Thermal Maximum (PETM)] and location of sites used in this study. IODP Site U1443 and ODP Site 758, forming the basis for this study, are highlighted by the large labeled yellow star; other deep sea sites are highlighted by labeled red circles; and onshore sites by labeled brown circles. Regions of potential deep water formation are schematically highlighted by dark blue polygons. NPDW = North Pacific Deep Water; SPDW = South Pacific Deep Water. Adapted from the Ocean Drilling Stratigraphic Network Paleomap Project (<http://www.odsnet.org/odsnet/services/paleomap/paleomap.html>; Hay et al., 1999). (For interpretation of the colors in the figure(s), the reader is referred to the web version of this article.)

tion of Laskar et al. (2011). Age model tie points and description are provided in Supplementary Information Section 5.0 and Table S1. Stable isotope and trace element records were generated for a 5 million year time interval spanning the peak of the Paleocene Carbon Isotope Maximum (PCIM) to the early Eocene (~58–53 Ma; Fig. 2b), with the aim of quantifying temperature and carbonate chemistry change during long-term warming towards peak Cenozoic warmth at the Early Eocene Climatic Optimum (EECO). We generated planktic stable isotope and trace element data from narrow sieve size fractions of the mixed-layer species *Morozovella velascoensis*/*M. subbotinae*-*marginodentata* plexus (250–300 μm) and the thermocline-dwelling *Subbotina velascoensis*/*S. hornibrooki* (212–250 μm). For benthic foraminifera, we used the shallow infaunal species *Oridorsalis umbonatus* for Mg/Ca and epifaunal species *Nuttallides truempyi* for B/Ca from the >150 μm fraction (Pearson et al., 2006; Brown et al., 2011; Lear et al., 2015). Since IODP Site U1443 and ODP Site 758 were located at a shallow paleo-depth of ~1,500 m during the early Paleogene, we note that benthic analyses from these sites reflect the temperature and carbonate saturation state of an intermediate depth water mass, rather than deep bottom waters of the Indian Ocean. See Supplementary Information Section 6.0 for further description and rationale concerning foraminifera picking.

$\delta^{13}\text{C}_{\text{bulk}}$ data were generated on a VG Optima Dual Inlet Mass Spectrometer at the NERC Isotope Geosciences Facility and a Sercon 20-22 Isotope Ratio Mass Spectrometer at the University of Exeter in continuous flow setup, with analytical error (2σ) of 0.06‰ for both instruments. Planktic stable isotope data were generated on a Thermo Finnigan MAT 253 Isotope Ratio Mass Spectrometer equipped with a Kiel IV Carbonate Preparation Device at Cardiff University, with long-term analytical precision (2σ) of 0.04‰ for $\delta^{13}\text{C}$ and 0.06‰ for $\delta^{18}\text{O}$. For trace element analysis, foraminifera were cleaned using both oxidative and reductive methods (modified from Boyle and Keigwin, 1985/86) and analyzed on a Thermo Finnigan Element XR Inductively-Coupled Plasma-Mass Spectrometer (ICP-MS) at the University of California Santa Cruz, following the methods of Brown et al. (2011). Long-term reproducibility of consistency standards indicates inter-run precision for Mg/Ca of <3% (2σ) and for B/Ca of <5% (2σ). The

complete stable isotope and trace element datasets supporting this manuscript have been archived online in the PANGAEA database: <https://doi.pangaea.de/10.1594/PANGAEA.910789>.

Non-thermal factors such as carbonate system (e.g. pH and carbonate ion concentration) and salinity exert a secondary influence on Mg/Ca in modern planktic foraminifera (Evans et al., 2016a). Paleogene records of ocean pH are reconstructed directly from carbonate $\delta^{11}\text{B}$ values (e.g., Penman et al., 2014; Babila et al., 2018), whereas estimation of carbonate ion requires an additional carbonate system parameter to be well-constrained or assumed. Temperatures were calculated from planktic Mg/Ca data using the following methodology outlined in Hollis et al. (2019). To limit the uncertainty introduced by different carbonate chemistry in the Paleogene ocean compared to the modern, planktic Mg/Ca data were pH-corrected using the linear correction of Evans et al. (2016a), based on long-term modeled pH values of 7.78–7.76 from Zeebe and Tyrrell (2019) and a $\delta^{11}\text{B}$ -based pH estimate of 7.67 for the PETM from Babila et al. (2018). Absolute temperatures were then calculated from the pH-corrected Mg/Ca data using the multi-species temperature calibration sensitivity of Anand et al. (2003). The evolution of early Eocene Mg/Ca_{sw} was taken from proxy data in Evans et al. (2018), with the mean early Eocene trend extrapolated linearly back into the Paleocene due to the paucity of late Paleocene proxy data. Absolute temperature estimates calculated using alternative models for the evolution of late Paleocene Mg/Ca_{sw}, along with an alternative temperature calibration (Evans et al., 2016b), are presented in Supplementary Information Section 11.0 (Figs. S7–S9). Benthic Mg/Ca data were converted to temperature using the species-specific temperature calibration of Lear et al. (2015) for the extant *O. umbonatus*. All published Mg/Ca temperature estimates included in the compilation figure in this manuscript were also recalibrated following the Hollis et al. (2019) approach summarized above to allow direct comparisons. Mixed layer seawater $\delta^{18}\text{O}$ ($\delta^{18}\text{O}_{\text{sw}}$) was calculated following Bemis et al. (1998), using Mg/Ca-derived temperatures and planktic $\delta^{18}\text{O}$ ($\delta^{18}\text{O}_{\text{planktic}}$) values from the same *Morozovella* spp. samples. Relative changes in carbonate chemistry (borate ion/DIC ratio; $\frac{[\text{B}(\text{OH})_4^-]}{[\text{DIC}]}$) were calculated from the planktic B/Ca data using the early Ceno-

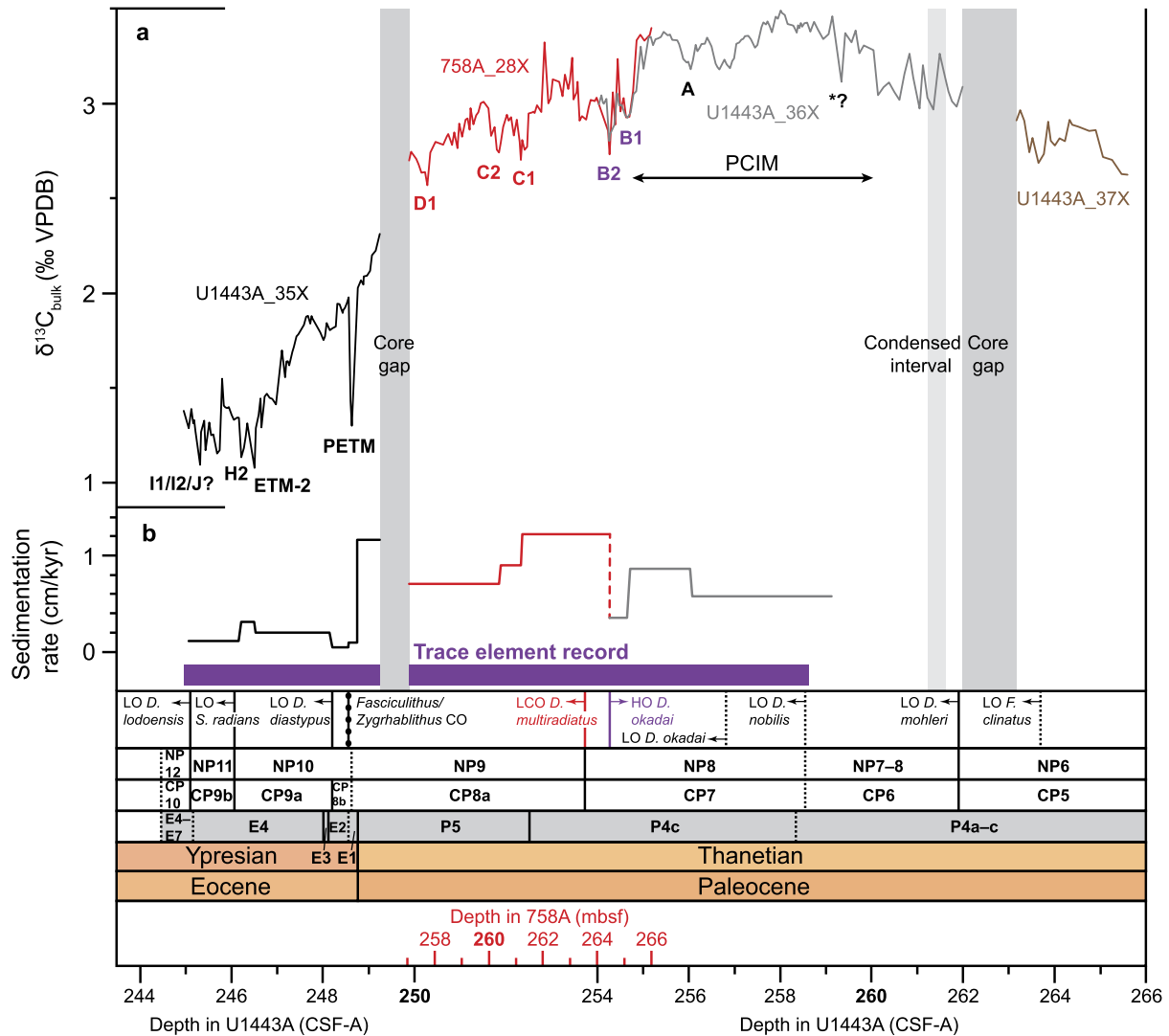


Fig. 2. Stratigraphy recovered by the splice between IODP Hole U1443A and ODP Hole 758A, plotted against depth in core and biostratigraphy. (a) $\delta^{13}\text{C}_{\text{bulk}}$ record, color-coded by core. Carbon cycle events are labeled below the $\delta^{13}\text{C}_{\text{bulk}}$ curve, with those at a low confidence indicated by a question mark. (b) Sedimentation rate and time interval encompassed by the trace element record. Carbon cycle and calcareous nannofossil biostratigraphic events occurring only within ODP Hole U1443A are indicated in black, events occurring only within ODP Hole 758A in red, and events occurring within both holes and forming key tie points in purple. LO = Lowest Occurrence; LCO = Lowest Common Occurrence; HO = Highest Occurrence; CO = Crossover. Core gaps and condensed intervals are indicated by vertical grey bars. PCIM = Paleocene Carbon Isotope Maximum.

zoic “low DIC” normalized calibration of Haynes et al. (2019). We compute relative changes as opposed to absolute values in order to minimize the influences of changing $\text{B}/\text{Ca}_{\text{sw}}$, which is poorly constrained across this time interval, and the assumption that modern sensitivities apply to extinct Paleogene taxa (Haynes et al., 2019). Relative changes in carbonate ion concentration ($\Delta[\text{CO}_3^{2-}]$) were calculated from the *N. truempyi* B/Ca data after Brown et al. (2011). See Supplementary Information Sections 11.0–15.0 for further description of temperature and carbonate chemistry calculations.

3. Results and discussion

3.1. Stratigraphy recovered by the splice

As shown in Fig. 2a, the new splice between IODP Hole U1443A and ODP Hole 758A recovers a significant portion of the late Paleocene–early Eocene stratigraphy from the onset of the Paleocene Carbon Isotope Maximum (PCIM) to the early Eocene. However, a section of the latest Paleocene stratigraphy encompassing the “D2” event, the younger negative $\delta^{13}\text{C}$ excursion of a double-

spiked carbon cycle perturbation in the latest Paleocene, is still missing. Based on a comparison of the $\delta^{13}\text{C}_{\text{bulk}}$ record to a stratigraphically complete $\delta^{13}\text{C}_{\text{bulk}}$ record from South Atlantic Walvis Ridge ODP Site 1262 (Zachos et al., 2005, 2010; Littler et al., 2014; Barnet et al., 2019), this interval of missing stratigraphy is unlikely to span more than ~ 400 kyr (i.e., one long eccentricity cycle).

Our new revised biostratigraphy indicates that our splice between Holes U1443A and 758A spans calcareous nannofossil biozones CP5 to CP10 (equivalent to NP6 to NP12) and planktic foraminiferal biozones P4a–c to E4, respectively. The highest occurrence (HO) of the calcareous nannofossil *Discoaster okadai* represents an important tie point in the splice between Cores U1443A-36X at 254.20 m CSF-A and 758A-28X at 264.57 mbsf. Biostratigraphic datums and depths are summarized in Tables 1 and 2. A significant decrease in sedimentation rate occurs across the Paleocene/Eocene boundary, from ~ 0.6 – 1.2 cm/kyr during the late Paleocene to ~ 0.1 – 0.3 cm/kyr during the early Eocene (Fig. 2b). As a result, carbon cycle events are assigned at a lower confidence level and 405-kyr orbital cyclicity is difficult to discern within the early Eocene portion of the $\delta^{13}\text{C}_{\text{bulk}}$ record (Fig. 2a).

Table 1

Calcareous nannofossil biostratigraphic datums for the IODP Hole U1443A/ODP Hole 758A splice. Biostratigraphic datums in IODP Hole U1443A are indicated in black font and those in ODP Hole 758A indicated in red font. LO = Lowest Occurrence; HO = Highest Occurrence; LCO = Lowest Common Occurrence; CO = Crossover.

Top interval Bottom interval (Hole_Core_Section_Depth)	Top depth Bottom depth (m; CSF-A/mbsf)	Mid-point depth (m; CSF-A/mbsf)	Nanno zone boundary	Biostratigraphic datum	Datum confidence
U1443A_35X_1_15.5 cm	245.055	245.10		LO <i>Discoaster lodoensis</i>	High
U1443A_35X_1_25 cm	245.15				
U1443A_35X_1_109 cm	245.99	246.07	Base NP12/CP10	LO <i>Sphenolithus radians</i>	High
U1443A_35X_1_125 cm	246.15				
U1443A_35X_3_24 cm	248.14	248.21	Base CP9a	LO <i>Discoaster diastypus</i>	High
U1443A_35X_3_37 cm	248.27				
U1443A_35X_3_37 cm	248.27	248.41		HO <i>Fasciculithus</i> spp.	High
U1443A_35X_3_65 cm	248.55				
U1443A_35X_3_65 cm	248.55	248.56		<i>Fasciculithus/Zygrhablithus</i> CO	High
U1443A_35X_3_72 cm	248.62				
758A_28X_2_91 cm	259.41	259.51		HO <i>Ericsonia robusta</i> (>9 μm)	High
758A_28X_2_111.5 cm	259.615				
758A_28X_4_37.5 cm	261.79	262.00		LO <i>Fasciculithus alanii</i>	High
758A_28X_4_79.5 cm	262.21				
758A_28X_5_54.5 cm	263.445	263.57	Base NP9/CP8a	LCO <i>Discoaster multiradiatus</i>	High
758A_28X_5_79 cm	263.69				
758A_28X_6_6.5 cm	264.465	264.57		HO <i>Discoaster okadai</i>	High
758A_28X_6_27.5 cm	264.675				
U1443A_36X_1_13 cm	254.13	254.20		HO <i>Discoaster okadai</i>	High
U1443A_36X_1_27 cm	254.27				
U1443A_36X_2_127.5 cm	256.775	256.83		LO <i>Discoaster okadai</i>	Low
U1443A_36X_2_139 cm	256.89				
U1443A_36X_3_147 cm	258.47	258.53	Base CP7	LO <i>Discoaster nobilis</i>	Low
U1443A_36X_4_8 cm	258.58				
U1443A_36X_6_35 cm	261.85	261.915	Base NP7/CP6	LO <i>Discoaster mohleri</i>	High
U1443A_36X_6_48 cm	261.98				
U1443A_37X_1_64.5 cm	263.64	263.70		LO <i>Fasciculithus clinatus</i>	Low
U1443A_37X_1_76 cm	263.76				

Table 2

Planktic foraminifer biostratigraphic datums for the IODP Hole U1443A/ODP Hole 758A splice. Biostratigraphic datums in IODP Hole U1443A are indicated in black font and in ODP Hole 758A in red font. B = Base. T = Top. Top depths for each sample given.

Top interval Bottom interval (Hole_Core_Section_Depth)	Top depth Bottom depth (m; CSF-A/mbsf)	Mid-point depth (m; CSF-A/mbsf)	Base of planktic foraminifera Zone	Datum
U1443A_35X_1_121-122 cm	246.11	246.67		T <i>Morozovella aequa</i>
U1443A_35X_2_82-83 cm	247.22			
U1443A_35X_3_40.5 cm	247.93	248.00	E4	B <i>Morozovella formosa</i>
U1443A_35X_3_53 cm	248.07			
U1443A_35X_3_40.5 cm	247.93	248.00		B <i>Morozovella lensiformis</i>
U1443A_35X_3_53 cm	248.07			
U1443A_35X_3_17-18 cm	248.07	248.11	E3	T <i>Morozovella velascoensis</i>
U1443A_35X_3_24-25 cm	248.14			
U1443A_35X_3_52-53 cm	248.42	248.52		B <i>Morozovella marginodentata</i>
U1443A_35X_3_72-73 cm	248.62			
U1443A_35X_3_72-73 cm	248.62	248.88	E1	B <i>Acarinina sibaiyaensis</i>
U1443A_35X_3_124.5-125.5 cm	249.15			
U1443A_35X_3_124.5-125.5 cm	249.15	250.15	P5	T <i>Globanomalina pseudomenardii</i>
U1443A_35X_CC	251.15			
758A_28X_3_53.5-54.5 cm	260.44	261.50	P5	T <i>Globanomalina pseudomenardii</i>
758A_28X_4_115-120 cm	262.55			
U1443A_36X_3_135-136 cm	258.35	260.28		B <i>Morozovella aequa</i>
U1443A_36X_CC	262.21			

The PETM is identifiable at 248.63 m CSF-A in IODP Hole U1443A by an abrupt negative excursion of $\sim 0.75\%$ in $\delta^{13}\text{C}_{\text{bulk}}$ and $\sim 1.7\%$ in $\delta^{13}\text{C}_{\text{planktic}}$. Biostratigraphically, this depth also corresponds to the appearance of the rare *Acarinina sibaiyaensis* which defines planktic foraminiferal Zone E1 which falls within the PETM, and the crossover between *Fasciculithus* and *Zygrhablithus*, quickly followed by the highest occurrence of *Fasciculithus* spp. within calcareous nannofossil zones CP8b/NP10 (Fig. 2; Tables 1 and 2). The PETM $\delta^{13}\text{C}$ excursion is defined in the IODP Hole U1443A record by only two data points, however, and since the negative excursion typically attains a magnitude of $\sim 2.5\text{--}3.0\%$ in marine carbonates (e.g., McNerney and Wing, 2011), it is likely that only a third to a half of the total magnitude of the PETM excursion is resolved

in our sample set. Similarly, the magnitude of the C1, C2, and D1 negative excursions are also smaller within the ODP Hole 758A $\delta^{13}\text{C}_{\text{bulk}}$ record compared to the ODP Site 1262 $\delta^{13}\text{C}_{\text{bulk}}$ record ($\sim 0.2\%$ at ODP Site 758 vs. $\sim 0.3\text{--}0.4\%$ at ODP Site 1262; Zachos et al., 2010), suggesting that the complete magnitude of these events has also not been captured due to the biscuiting and/or low sedimentation rates ($\sim 0.7\text{--}1.2$ cm/kyr) in the ODP Hole 758A core.

3.2. Long-term Indian Ocean temperature and $\delta^{18}\text{O}_{\text{sw}}$ evolution

A long-term rise in foraminiferal Mg/Ca values from the late Paleocene to early Eocene is observed at all depths within the water column (Fig. 3). These increasing Mg/Ca values equate to a $\sim 4^\circ\text{C}$

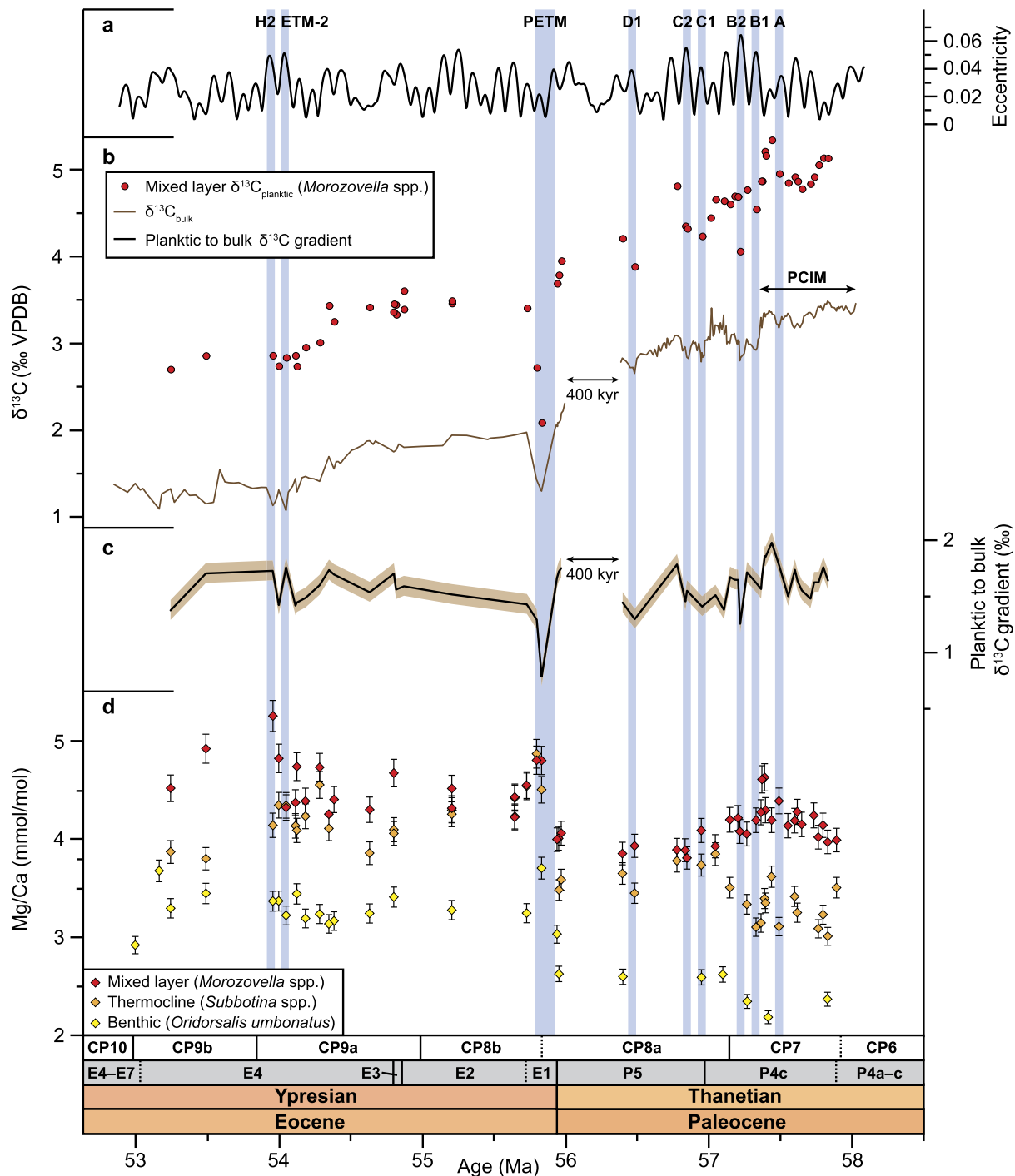


Fig. 3. Raw Mg/Ca data for mixed layer, thermocline, and intermediate water depths plotted against age. (a) La2010b orbital solution (Laskar et al., 2011). (b) IODP Hole U1443A/ODP Hole 758A $\delta^{13}\text{C}_{\text{bulk}}$ and $\delta^{13}\text{C}_{\text{planktic}}$ records with latest Paleocene core gap indicated. PCIM = Paleocene Carbon Isotope Maximum. (c) Planktic to bulk $\delta^{13}\text{C}$ gradient with latest Paleocene core gap indicated. Pale brown shading represents uncertainty ($\pm 0.1\%$), based on the analytical uncertainty on the $\delta^{13}\text{C}_{\text{planktic}}$ and $\delta^{13}\text{C}_{\text{bulk}}$ measurements. (d) Raw Mg/Ca data for the IODP Hole U1443A/ODP Hole 758A splice, color coded by genus/depth habitat. Error bars indicate analytical uncertainty on the Mg/Ca measurements ($\pm 3\%$). See Supplementary Figs. S1 and S2 for planktic $\delta^{13}\text{C}$ and Mg/Ca data plotted by foraminiferal species.

warming of mixed layer and bottom waters and $\sim 5^\circ\text{C}$ at thermocline depths between 58 and 53 Ma (Fig. 4). Increasing ocean temperatures are accompanied by rising mixed layer $\delta^{18}\text{O}_{\text{sw}}$ of $\sim 0.8\%$, suggesting a long-term increase in net evaporation (i.e., increase in surface ocean salinity) in the low latitude Indian Ocean in response to climatic warming (Fig. 4c), assuming an ice-free world. It is important to note that a portion of this apparent $\delta^{18}\text{O}_{\text{sw}}$ rise could also be explained by a decrease in surface ocean pH (Zeebe and Tyrrell, 2019).

However, the rate of warming is not consistent across the records, nor within different parts of the water column. For instance, the temperature gradient between the mixed layer-dwelling and thermocline-dwelling species collapses at ~ 57 Ma (Fig. 4b). This apparent convergence in the data could be explained by two different scenarios. The first scenario involves a significant expansion of the mixed layer during this time, such that from 57 Ma thermocline-dwelling *Subbotina* are effectively living within the lower part of the mixed layer in a water mass of a

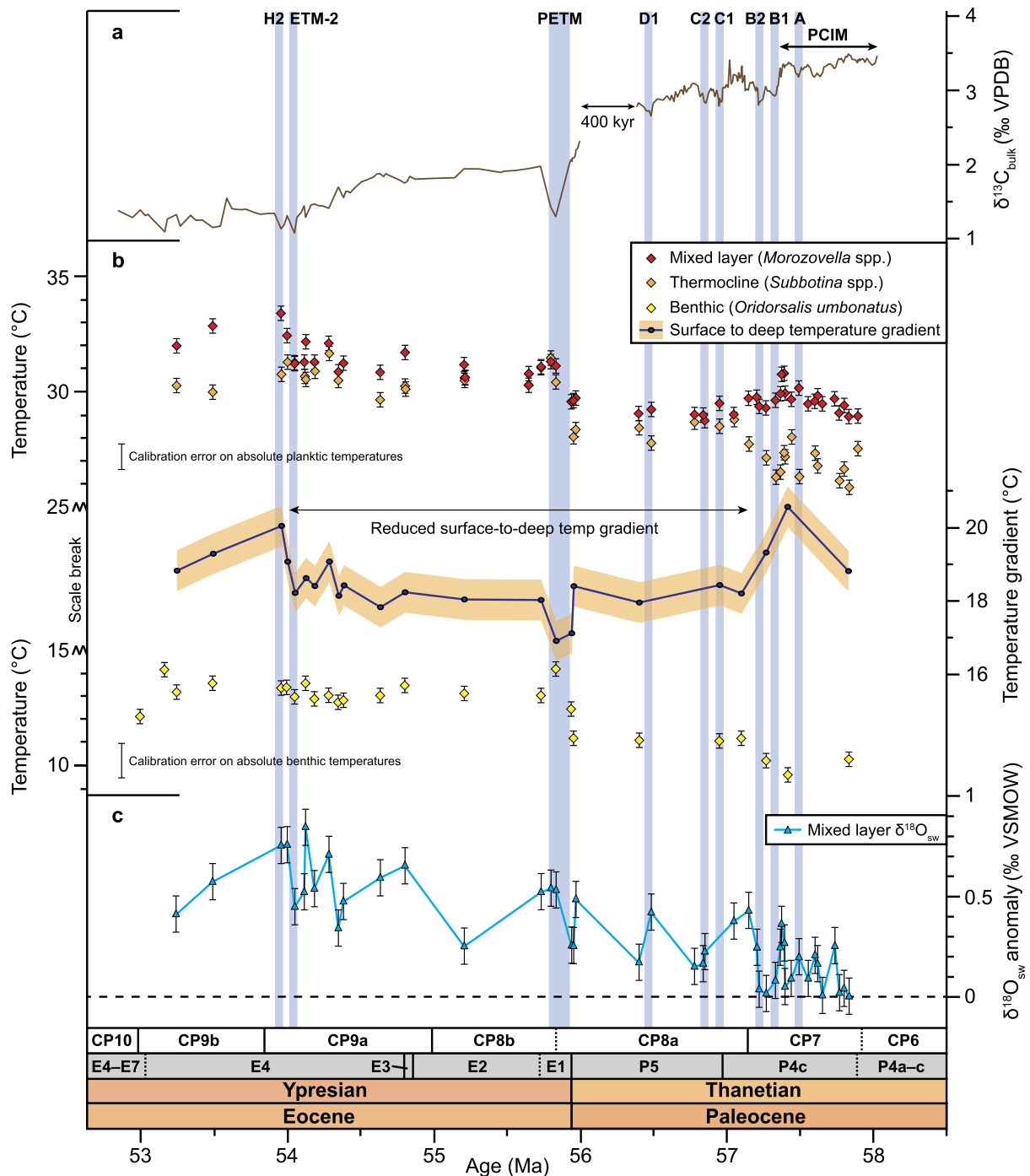


Fig. 4. Mg/Ca temperature records for mixed layer, thermocline, and intermediate water depths plotted against age, with bulk carbon isotope values for context. (a) IODP Hole U1443A/ODP Hole 758A $\delta^{13}\text{C}_{\text{bulk}}$ record, with latest Paleocene core gap indicated. PCIM = Paleocene Carbon Isotope Maximum. (b) Mg/Ca temperature records for the IODP Hole U1443A/ODP Hole 758A splice, color coded by depth habitat. Surface-to-deep (mixed layer to intermediate water depth) temperature gradient also indicated. Error bars on the temperature measurements indicate analytical uncertainty on the Mg/Ca measurements ($\pm 0.3^\circ\text{C}$). Mixed layer and thermocline absolute temperatures are also associated with a calibration error of $\pm 1.13^\circ\text{C}$ (Anand et al., 2003) and benthic absolute temperatures with a calibration error of $\pm 1.5^\circ\text{C}$ (Lear et al., 2015). Additional sources of uncertainty, which are more challenging to constrain, arise from modeled pH and Mg/Ca_{sw} values for the late Paleocene to early Eocene. Temperatures calculated using a range of modeled Mg/Ca_{sw} scenarios for the poorly constrained late Paleocene, and an alternative temperature calibration (Evans et al., 2016b), are shown in Supplementary Figs. S7–S9. A conservative error window on the surface-to-deep temperature gradient was calculated by propagating analytical uncertainties on the mixed layer and benthic temperature estimates. (c) Mixed layer $\delta^{18}\text{O}_{\text{sw}}$ record, plotted as an anomaly relative to a baseline of 0 for peak PCIM conditions. Error bars are based on propagating the analytical uncertainties associated with the Mg/Ca ($\pm 0.3^\circ\text{C}$) and $\delta^{18}\text{O}_{\text{planktic}}$ ($\pm 0.06\text{‰}$) measurements.

comparable temperature to *Morozovella*. This model assumes that long-term late Paleocene warming created a more homogeneous water column with a thicker mixed layer and a deeper thermocline characterized by a lower temperature gradient, in response to enhanced atmospheric circulation, storm activity, and polar ampli-

fication of warming. Such a scenario has been invoked for transient rapid warming during the PETM (e.g., Makarova et al., 2017), and is supported within this dataset by the greater magnitude of warming at both thermocline and intermediate water depths compared to the mixed layer ~ 57 Ma (Fig. 4b). Furthermore, convergence

between the mixed layer and thermocline Mg/Ca data is also accompanied by a step-like rise in mixed layer $\delta^{18}\text{O}_{\text{sw}}$ (Fig. 4c), suggesting an increase in net evaporation and surface ocean salinity, which may have promoted a thickening of the mixed layer in response to downwelling of saltier, denser surface waters (e.g., Tripathi et al., 2003). The second scenario involves a deepening of the *Morozovella* depth habitat in response to mixed layer warming. Depth migration has been commonly invoked for individual species during the PETM (e.g., Si and Aubry, 2018), and depth migrations of planktic foraminifera in response to longer term warming have been documented from the Oligocene (Matsui et al., 2016). Habitat deepening for the *Morozovella* is potentially supported by the observation that most of the apparent temperature convergence is a result of a significant warming within the *Subbotina* data, while the *Morozovella* data exhibit little change or even a small decrease in temperature. Therefore, while the *Subbotina* record a warming of $\sim 2.5^\circ\text{C}$, the *Morozovella* record a cooling of $\sim 0.5^\circ\text{C}$ around 57 Ma (albeit within analytical uncertainty of the Mg/Ca measurements). However, this argument is complicated by the negligible change in gradient between the *Morozovella* and bulk carbonate carbon isotope records across this time interval (Fig. 3c). Similarly, absolute *Morozovella* $\delta^{13}\text{C}$ values do not exhibit a step change to more negative values ~ 57 Ma, but largely fall close to analytical uncertainty of each other outside of major carbon cycle perturbations such as the B2 event (Fig. 3b). Intriguingly, typical mixed-layer and thermocline-dwelling foraminifera in the modern sub-tropical Indian Ocean are characterized by comparable Mg/Ca values to one another, because they both inhabit a narrow depth range (~ 73 – 109 m) just below the mixed layer that corresponds to the deep chlorophyll maximum (Stainbank et al., 2019). In the modern Indian Ocean, this similarity is controlled by a common depth habitat related to food supply (Stainbank et al., 2019), whilst the evolution of similar geochemical signatures during the late Paleocene–early Eocene may be related to either changing physical properties of the water mass or depth migration of the *Morozovella* (Makarova et al., 2017; Si and Aubry, 2018).

Furthermore, there is a ~ 1 million year period of relative stability within the mixed layer, thermocline, and benthic Mg/Ca temperature records during the latest Paleocene from ~ 57 – 56 Ma, superimposed on the long-term late Paleocene–early Eocene warming trend (Fig. 4b). However, the benthic data are of low resolution through this time interval due to a paucity of benthic specimens for analysis. Since the evolution of late Paleocene Mg/Ca_{sw} is poorly constrained and is a required parameter for the calculation of absolute temperatures from planktic Mg/Ca data, it is possible that a larger decrease in Mg/Ca_{sw} than modeled during this interval could account for the apparent stability in the *Morozovella* and *Subbotina* records. Temperatures have also been calculated assuming two alternative models for the evolution of late Paleocene Mg/Ca_{sw} in Supplementary Information Section 11.0 (Fig. S7): one assuming constant late Paleocene Mg/Ca_{sw} of 2.6 mol/mol [consistent with PETM proxy data in Evans et al. (2018)], and one assuming increasing late Paleocene Mg/Ca_{sw} [consistent with low resolution proxy data based on corals in Gothmann et al. (2015)]. Whilst these alternative models for the late Paleocene do not affect the long-term early Eocene warming trend, the increasing late Paleocene Mg/Ca_{sw} model in particular exaggerates a gradual latest Paleocene cooling trend towards the PETM, which is inconsistent with high-resolution $\delta^{18}\text{O}_{\text{benthic}}$ temperature records across this time interval from the Atlantic and Pacific (Littler et al., 2014; Westerhold et al., 2018; Barnet et al., 2019). The resulting temperature trends from our planktic Mg/Ca data therefore support a scenario of decreasing Mg/Ca_{sw} during the late Paleocene time interval considered here, although further proxy data are required to determine the magnitude of this Mg/Ca_{sw} change.

The Mg/Ca-derived temperature records display a step-like shift to warmer baseline temperatures throughout the water column during and following the PETM, which is particularly evident in the benthic (*O. umbonatus*) and thermocline (*Subbotina* spp.) records (Fig. 4b). As a consequence of enhanced warming during the PETM at thermocline and intermediate water depths, there is a reduction in the surface-to-deep thermal gradient during the PETM, which persisted for at least 2 million years into the early Eocene in the Indian Ocean (Fig. 4b). A decreasing surface-to-deep temperature gradient from the late Paleocene to the early Eocene has also been interpreted at other low latitude sites such as ODP Site 1209 in the central Pacific, based on lower resolution planktic and benthic $\delta^{18}\text{O}$ records (Dutton et al., 2005). The temperature gradient decrease at ODP Site 1209 also occurred primarily as the result of a greater magnitude of deep water warming, suggesting that a reduction in the surface-to-deep temperature gradient was characteristic of both the low latitude Indian and Pacific oceans during global late Paleocene–early Eocene warming.

By comparing our new mixed layer Mg/Ca-derived temperature data to published latest Paleocene surface water temperature estimates from the low latitudes and equatorial regions, it becomes evident that relatively stable temperatures are characteristic of the global low latitudes at this time (Fig. 5). Absolute temperature estimates based on the $\text{TEX}_{86}^{\text{H}}$ proxy are notably warmer than other temperature proxies by ~ 2 – 3°C , perhaps due to seasonal bias, or to issues with the $\text{TEX}_{86}^{\text{H}}$ calibration (e.g., Eley et al., 2019). Importantly, our new Indian Ocean Mg/Ca dataset captures a long-term early Eocene warming trend in the low latitude mixed layer that had otherwise only been observed at equatorial Pacific ODP Site 865 (Tripathi et al., 2003; Tripathi and Elderfield, 2004), corroborating data from this site and indicating that the thermal histories between the low latitude Indian and Pacific Oceans were coupled over this interval.

Warming of intermediate to deep water masses within the Indian, central Pacific, South Atlantic, and Southern Oceans through the late Paleocene and early Eocene suggests significant warming within the high latitude regions of intermediate to deep water formation (Fig. 5b). However, intermediate waters of the Indian Ocean at $\sim 1,500$ m depth are initially generally warmer by ~ 0.5 – 1.5°C , likely due to a shallower paleodepth compared to other studied sites ($\sim 2,500$ – $3,500$ m; Lear et al., 2015; Westerhold et al., 2018; Barnet et al., 2019). However, the Indian Ocean intermediate-depth temperature record converges with the deeper bottom water records from the Atlantic, Pacific, and Southern Ocean during the early Eocene after ETM-2, supporting polar amplification of early Eocene greenhouse warming (assuming high latitude bottom water sources at this time; Thomas et al., 2008; Cramwinckel et al., 2018). However, at this stage we cannot rule out the possibility that this apparent convergence may be an artefact of poorer age control in the more condensed early Eocene portion of the Indian Ocean record (Fig. 2).

More broadly, synchronous long-term warming within both the low and high latitudes from the late Paleocene to early Eocene, as well as within all three major ocean basins, supports suggestions that global climate was principally forced by changes in greenhouse gas concentrations during this time, as opposed to significant changes in thermohaline circulation (e.g., Cramwinckel et al., 2018). Changes in the strength and mode of thermohaline circulation, forced by the opening and closing of ocean gateways or changes in the locations of deep water formation, can have a significant impact on climate at the local and regional scale, especially in high latitude regions characterized by low levels of solar insolation. However, while changes in thermohaline circulation can lead to an effective redistribution of heat, such changes alone cannot explain global warming throughout the world ocean at both low and high latitudes, although transient changes in thermohaline

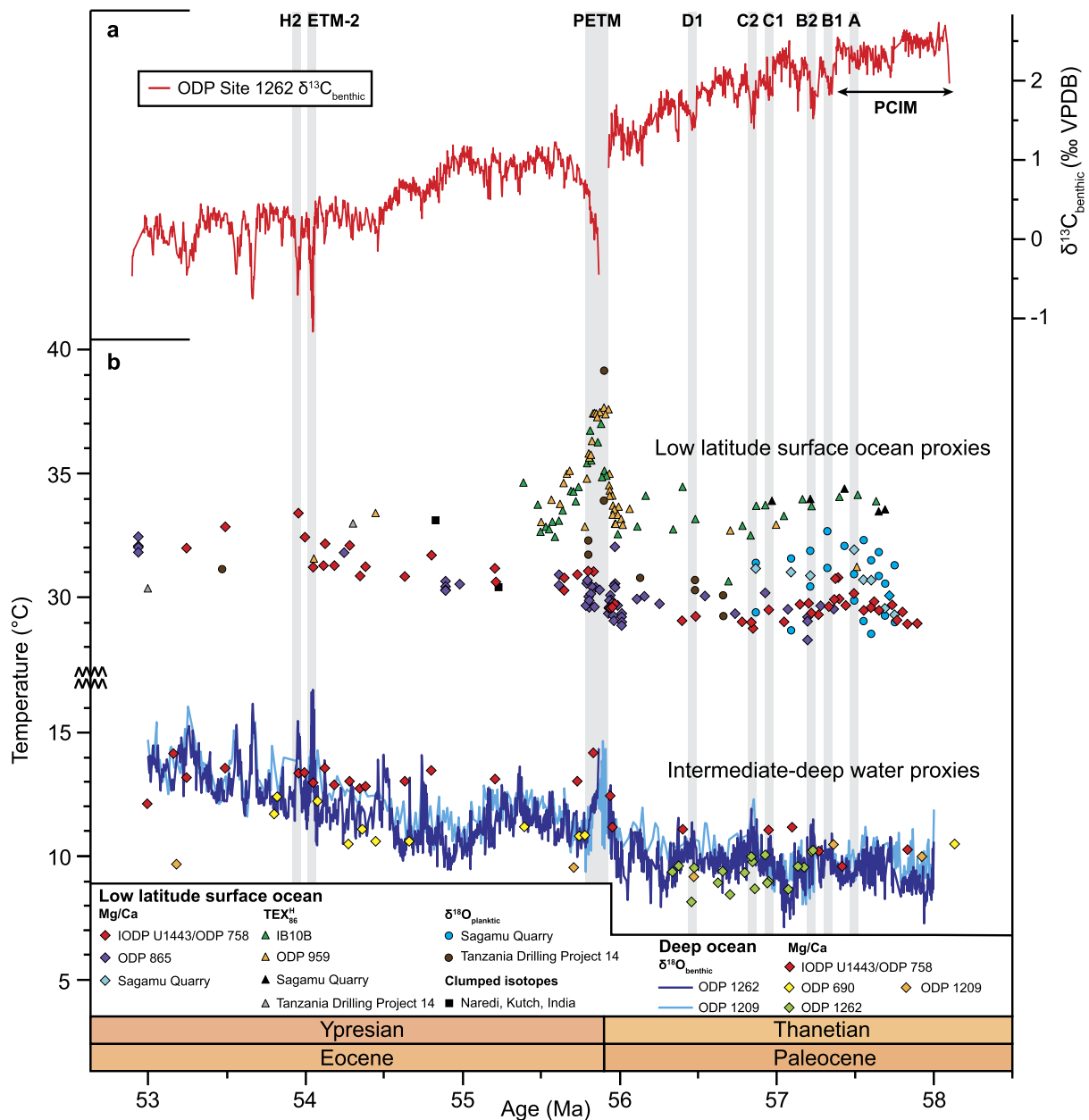


Fig. 5. Compilation of published temperature proxy data from the low latitude surface ocean and deep ocean, plotted on the age model generated during this study. (a) High-resolution benthic carbon isotope ($\delta^{13}\text{C}_{\text{benthic}}$) record from ODP Site 1262 (Littler et al., 2014; Lauretano et al., 2015; Barnett et al., 2019). PCIM = Paleocene Carbon Isotope Maximum. (b) New Mg/Ca temperature records from the Indian Ocean (red diamonds, this study) plotted against published low latitude surface ocean temperature proxy data and deep ocean temperature proxy data. See Fig. 1 for site locations and Supplementary Table S2 for the sources of all published data. All published Mg/Ca temperature estimates included in this figure were recalibrated following the Hollis et al. (2019) approach used in this study. However, temperature estimates based on other proxies remain unchanged from the original literature source. All $\text{TEX}_{86}^{\text{H}}$ temperatures are plotted using the $\text{TEX}_{86}^{\text{H}}$ calibration (Kim et al., 2010).

circulation may have occurred during the early Paleogene as a consequence of greenhouse gas-forced climate change (e.g., Thomas, 2004; Nunes and Norris, 2006; Thomas et al., 2008; Hague et al., 2012). While not the focus of this study, at present the most likely driver of such increasing atmospheric greenhouse gas concentrations appears to be the second and major phase of volcanism within the North Atlantic Igneous Province (NAIP) from ~57.5–54 Ma (Wilkinson et al., 2016; Greene et al., 2019).

Our new temperature proxy data from the Indian Ocean and low latitude temperature proxy data compilation are compared to modeled meridional sea surface temperature (SST) gradients based on the late Paleocene National Center for Atmospheric Research Community Earth System Model (NCAR CESM1), assuming a radiative forcing equivalent to 2240 ppm CO_2 (Frieling et al., 2017), the

FAMOUS Model E17 simulation (Sagoo et al., 2013), assuming a radiative forcing equivalent to 560 ppm CO_2 , and modern meridional gradients (Locarnini et al., 2013) in Fig. 6. We use benthic temperature estimates from IODP Site U1443/ODP Site 758 (~1500 m paleo-depth) and ODP Site 1262 (~3500 m paleo-depth) as crude estimates for high latitude SSTs at $>60^\circ\text{S}$, as early Paleogene deep waters in the South Atlantic and Indian oceans were predominantly formed in the Southern Ocean (e.g., Thomas et al., 2008).

Our new late Paleocene Mg/Ca-derived temperature estimates from IODP Site U1443/ODP Site 758 (~29–31 °C) represent a good fit to modeled SSTs of ~30 °C by the NCAR CESM1 model at ~29°S, and are significantly warmer than modern mean annual temperatures (~15–25 °C) and maximum summer temperatures (~25–27 °C) at this latitude (Fig. 6a). However, our early

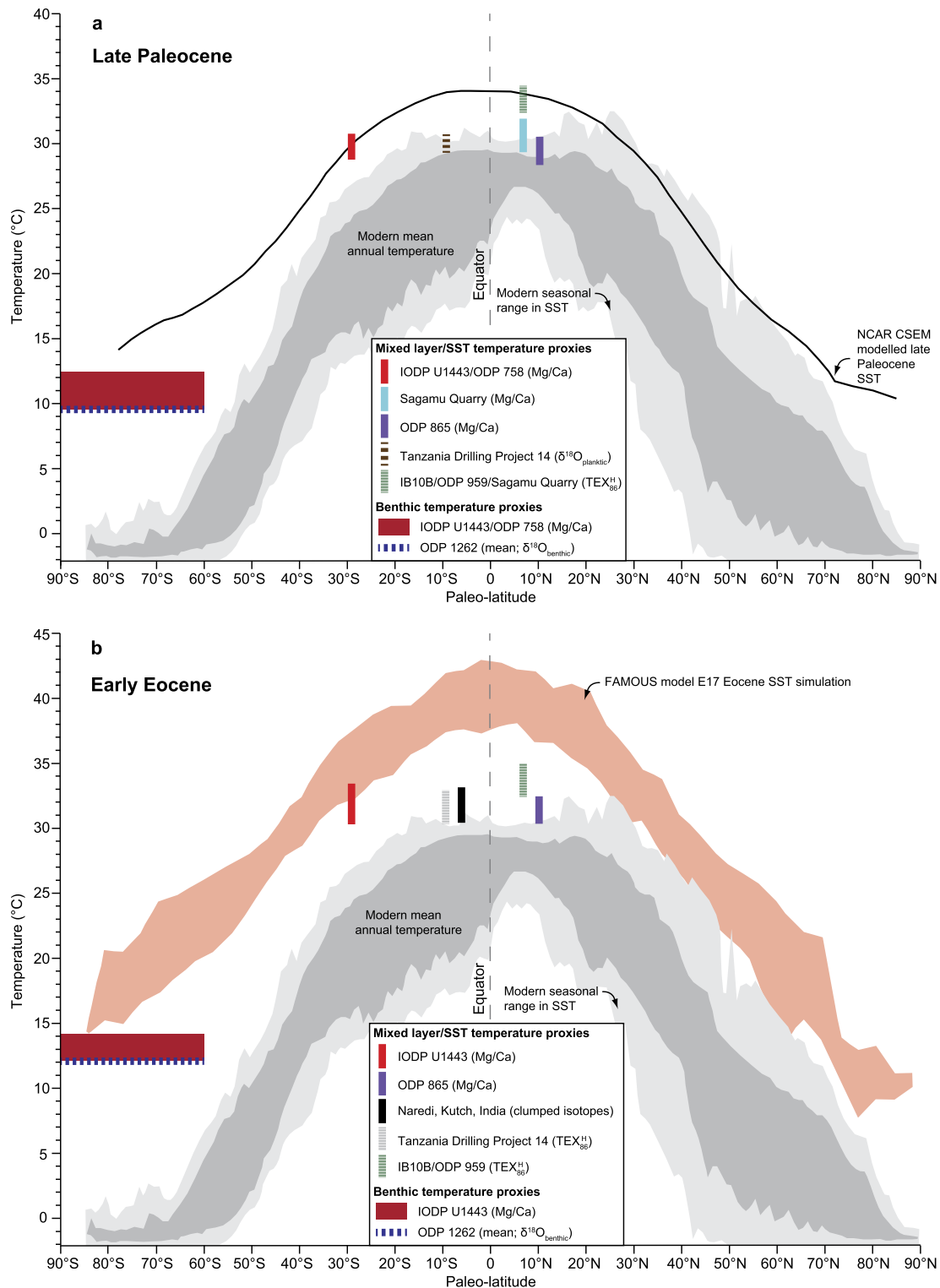


Fig. 6. Comparison between proxy data and modeling results for late Paleocene–early Eocene sea surface temperature (SST), with modern mean annual temperature and seasonal range in SST also shown for comparison (Locarnini et al., 2013). (a) Late Paleocene temperature proxy data plotted against the modeled meridional SST gradient based on the National Center for Atmospheric Research Community Earth System Model (NCAR CESM1) from Frieling et al. (2017), assuming a radiative forcing equivalent to 2240 ppm CO_2 . (b) Early Eocene temperature proxy data plotted against the modeled meridional SST gradient based on the FAMOUS Model E17 Eocene simulation from Sagoo et al. (2013), assuming a radiative forcing equivalent to 560 ppm CO_2 . All low latitude surface ocean and benthic IODP Site U1443/ODP Site 758 temperature proxy data are plotted as ranges of values for the late Paleocene and early Eocene in (a) and (b) respectively, while mean late Paleocene and early Eocene temperatures are plotted for ODP Site 1262. PETM proxy data are considered anomalous and have been excluded. Paleo-latitudes for the low latitude sites were computed relative to the paleomagnetic reference frame of Torsvik et al. (2012), using Version 2.1 of the model from paleolatitudes.org (Van Hinsbergen et al., 2015). Benthic temperature proxy data from IODP Site U1443/ODP Site 758 (~1500 m paleo-depth) and ODP Site 1262 (~3500 m paleo-depth) are interpreted as crude estimates for high southern latitude SSTs at $>60^\circ\text{S}$, as early Paleogene deep waters in the South Atlantic and Indian oceans were predominantly formed in the Southern Ocean. See Fig. 1 for site locations and Supplementary Table S2 for the sources of all published data. All published Mg/Ca temperature estimates included in this figure were recalibrated following the Hollis et al. (2019) approach used in this study. However, temperature estimates based on other proxies remain unchanged from the original literature source. All $\text{TEX}_{86}^{\text{H}}$ temperatures are plotted using the $\text{TEX}_{86}^{\text{H}}$ calibration (Kim et al., 2010).

Eocene temperature estimates ($\sim 30\text{--}33^\circ\text{C}$) are generally cooler than modeled by the FAMOUS Model E12 simulation ($\sim 32\text{--}37^\circ\text{C}$; Fig. 6b). While the NCAR CESM1 model simulates a significantly reduced equator-pole temperature gradient compared to the modern, supporting polar amplification of early Paleogene greenhouse warming as suggested by our proxy data compilation, both model outputs appear to overestimate absolute temperature estimates in equatorial and polar regions, especially those determined by foraminiferal Mg/Ca and $\delta^{18}\text{O}$. A portion of this discrepancy in equatorial regions could be attributed to the fact that planktic foraminifera such as *Morozovella* record an integrated mixed layer signal ($\sim 0\text{--}30$ m depth), rather than true SST (Frieling et al., 2017). Furthermore, our temperature proxy record does not extend to peak warmth of EECO ($\sim 53\text{--}49$ Ma), when the warmest ambient temperatures of the early Eocene, and indeed the entire Cenozoic, occurred (Westerhold et al., 2018; Barnet et al., 2019). Meanwhile, in the high southern latitudes, early Paleogene deep water formation in the Southern Ocean may have predominantly taken place during winter when surface waters were colder and denser, biasing deep water temperatures in the Atlantic and Indian oceans to cooler values than annual mean SSTs in the Southern Ocean (Hollis et al., 2012).

3.3. Long-term Indian Ocean carbonate chemistry evolution

Greenhouse gas forcing of long-term global warming during the late Paleocene–early Eocene should have initiated changes to the carbonate chemistry of the global ocean. Assuming the “low DIC” calibration of Haynes et al. (2019), our observed long-term decrease in mixed layer B/Ca ratios of ~ 30 $\mu\text{mol/mol}$ would equate to a decrease in $\frac{[\text{B}(\text{OH})_4^-]}{\text{DIC}}$ of ~ 0.02 (Fig. 7). The long residence time of B (i.e., 11–17 Myr; Lemarchand et al., 2002) indicates that total [B] are unlikely to have changed significantly over our study interval; we therefore suggest that either a decrease in pH and/or increase in DIC of the mixed layer is a more likely scenario to explain the $\frac{[\text{B}(\text{OH})_4^-]}{\text{DIC}}$ change. This explanation is therefore consistent with increasing atmospheric CO_2 during this time. However, the long-term decrease in B/Ca is comparatively muted at thermocline relative to mixed layer depths (Fig. 7b). This may indicate a lower sensitivity of B/Ca to the carbonate system in the thermocline-dwelling *Subbotina* compared to the mixed layer-dwelling *Morozovella*, by analogy with lower sensitivity in modern deeper-dwelling taxa (e.g., Haynes et al., 2019). Alternatively, the larger B/Ca response in the *Morozovella* could support a deepening of this genus’ habitat into more corrosive waters over time, or reflect a change in the pH gradient between the mixed-layer and thermocline waters, resulting from significantly shallower depths of organic carbon remineralization in the hotter late Paleocene–early Eocene oceans (John et al., 2014).

A long-term fall in B/Ca is also evident in the benthic B/Ca record (Fig. 7b), equating to a long-term drop in carbonate ion concentration of ~ 20 $\mu\text{mol/kg}$ of the intermediate water mass bathing the crest of Ninetyeast Ridge (Fig. 7d). Although many proxy and modeling studies suggest a deepening CCD from the late Paleocene to early Eocene within the Atlantic, Pacific, and Indian Oceans (Komar et al., 2013; Slotnick et al., 2015), a recent study by Greene et al. (2019) revealed no statistically significant CCD deepening during this interval. This apparent discrepancy is consistent with our data, which records the chemistry of a shallower intermediate depth water mass ($\sim 1,500$ m depth), whose properties may differ from that of the bottom water mass in the Indian Ocean that controlled the position of the CCD (at $\sim 3,500\text{--}4,500$ m water depth) during the early Paleogene (Slotnick et al., 2015).

3.4. Late Paleocene orbital cyclicity

In high-resolution benthic stable isotope records from the South Atlantic Walvis Ridge ODP Site 1262, late Paleocene long (405-kyr) eccentricity maxima are associated with transient bottom water warming of $\sim 1\text{--}2^\circ\text{C}$ and negative excursions in $\delta^{13}\text{C}$, suggesting global warming and release of temperature-sensitive isotopically light carbon (CO_2 or CH_4) reservoirs as a positive feedback response to an initial warming induced by orbital forcing (Littler et al., 2014; Barnet et al., 2019). The resolution of the late Paleocene portion of the stable isotope and trace element records is sufficiently high that the imprint of 405-kyr cyclicity can be potentially resolved in the $\delta^{13}\text{C}_{\text{bulk}}$ and planktic stable isotope and trace element records, superimposed on the longer term changes in temperature and carbonate chemistry (Fig. 8). However, changes on orbital timescales are more difficult to discern within the benthic data, since benthic B/Ca values generally vary largely within analytical uncertainty (Fig. 8b), while the benthic Mg/Ca record lacks the required resolution to resolve orbital-scale changes during the late Paleocene (Fig. 3d).

The imprint of orbital cyclicity is expressed within the late Paleocene $\delta^{13}\text{C}_{\text{bulk}}$ record and also appears to exhibit an expression within the mixed layer B/Ca record, with each 405-kyr maximum characterized by decreases in $\delta^{13}\text{C}_{\text{bulk}}$ and B/Ca beyond analytical uncertainty, suggesting a transient fall in pH and/or increase in DIC as a result of the transient release of greenhouse gases into the exogenic carbon cycle from temperature sensitive carbon stores such as peat, permafrost, or methane hydrates (Fig. 8d; Littler et al., 2014; Barnet et al., 2019). By contrast, orbitally-paced variations in mixed layer temperature are less pronounced and generally fall within analytical uncertainty of the Mg/Ca measurements ($\pm 0.3^\circ\text{C}$) (Fig. 8c). The lack of evidence for 405-kyr cyclicity within the mixed layer Mg/Ca record may be due to the combination of a relatively small temperature change ($\sim 1\text{--}2^\circ\text{C}$) on such orbital timescales, coupled with the fact that the complete magnitude of these events has not been captured owing to the low sedimentation rates and biscuiting within the IODP Site U1443/ODP Site 758 core.

The PETM interval captured within the trace element records is characterized by mixed layer warming within IODP Hole U1443A of $\sim 1.5^\circ\text{C}$, from ~ 29.5 (± 1.4) $^\circ\text{C}$ during the latest Paleocene to ~ 31.0 (± 1.4) $^\circ\text{C}$ during the PETM recovery, less than half of the total warming ($\sim 4^\circ\text{C}$) recorded at the more complete, low latitude ODP Site 1209 (Penman et al., 2014; Zachos et al., 2003). Furthermore, the decrease in mixed layer B/Ca across the PETM of ~ 8 $\mu\text{mol/mol}$ equates to between a quarter and a third of the B/Ca excursion within more complete PETM records from the equatorial Pacific and Southern Oceans ($\sim 25\text{--}30$ $\mu\text{mol/mol}$; Babila et al., 2018). The reduced magnitude of the excursions in Mg/Ca and B/Ca are consistent with biostratigraphic and chemostratigraphic evidence suggesting that only a third to a half of the complete magnitude of the PETM excursion has been captured within our record.

4. Conclusions

We present the first sub-eccentricity-resolution long-term late Paleocene–early Eocene trace element records across a depth transect through the water column of the low latitude Indian Ocean. This record resolves late Paleocene 405-kyr orbital cycles and a portion of the PETM, and sheds light on the multi-million year evolution of temperature and carbonate chemistry in this region for the first time. We observe a long-term warming of $\sim 4\text{--}5^\circ\text{C}$ at all water depths from ~ 58 to 53 Ma in the northern In-

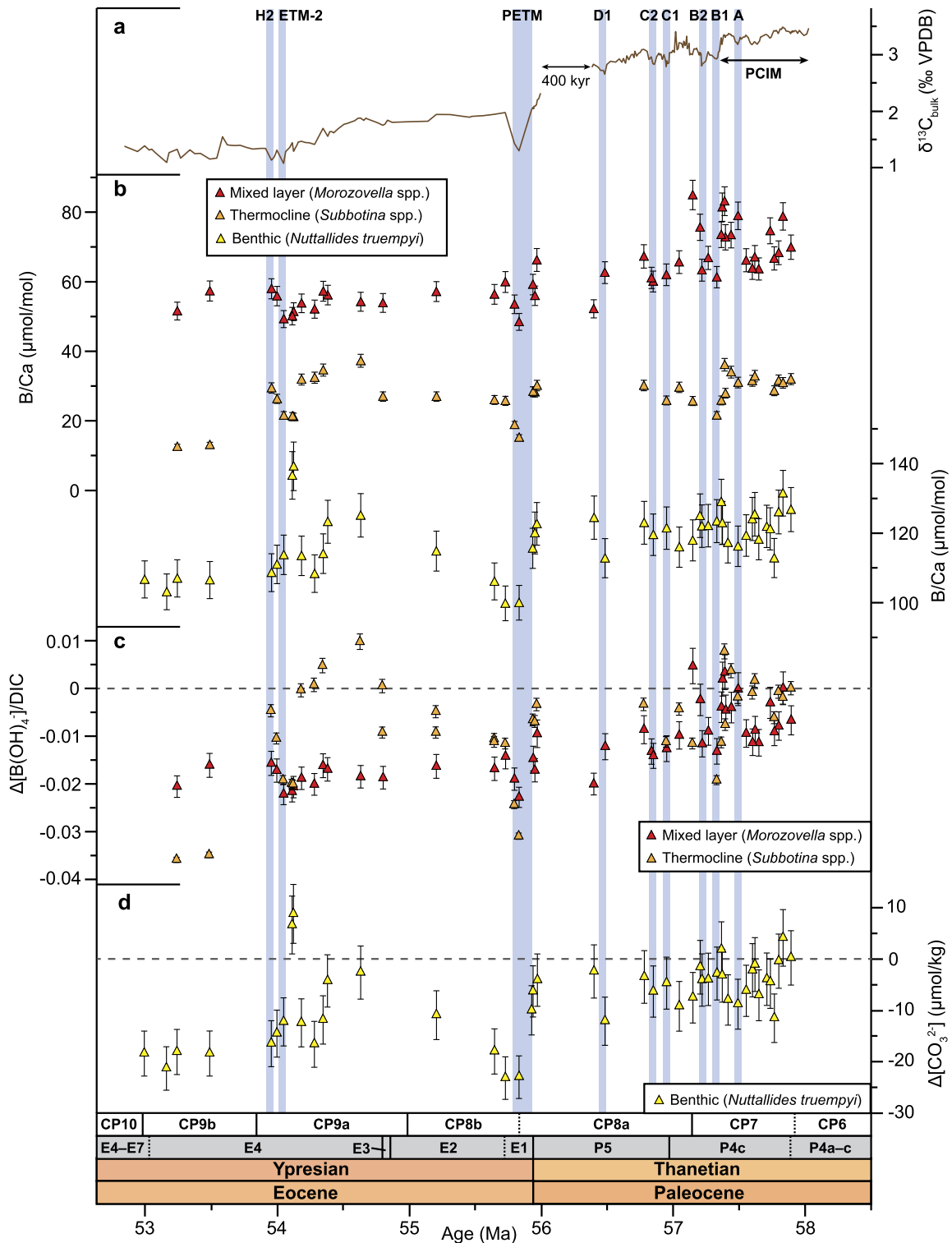


Fig. 7. Raw B/Ca data and carbonate chemistry for mixed layer, thermocline, and intermediate water depths plotted against age. (a) IODP Hole U1443A/ODP Hole 758A $\delta^{13}\text{C}_{\text{bulk}}$ record, with latest Paleocene core gap indicated. PCIM = Paleocene Carbon Isotope Maximum. (b) Raw B/Ca data for the IODP Hole U1443A/ODP Hole 758A splice, color-coded by depth habitat. Error bars indicate analytical uncertainty on the B/Ca measurements ($\pm 5\%$). (c) Change in mixed layer and thermocline carbonate chemistry (borate ion/dissolved inorganic carbon ratio; $\Delta[\text{B}(\text{OH})_4^-]/\text{DIC}$), plotted as the change relative to a baseline of 0 for peak PCIM conditions. (d) Change in benthic (intermediate water depth) carbonate chemistry (carbonate ion concentration; $\Delta[\text{CO}_3^{2-}]$), plotted as the change relative to a base line of 0 for peak PCIM conditions. Error bars on the carbonate chemistry data points indicate propagated analytical uncertainties associated with the B/Ca data points.

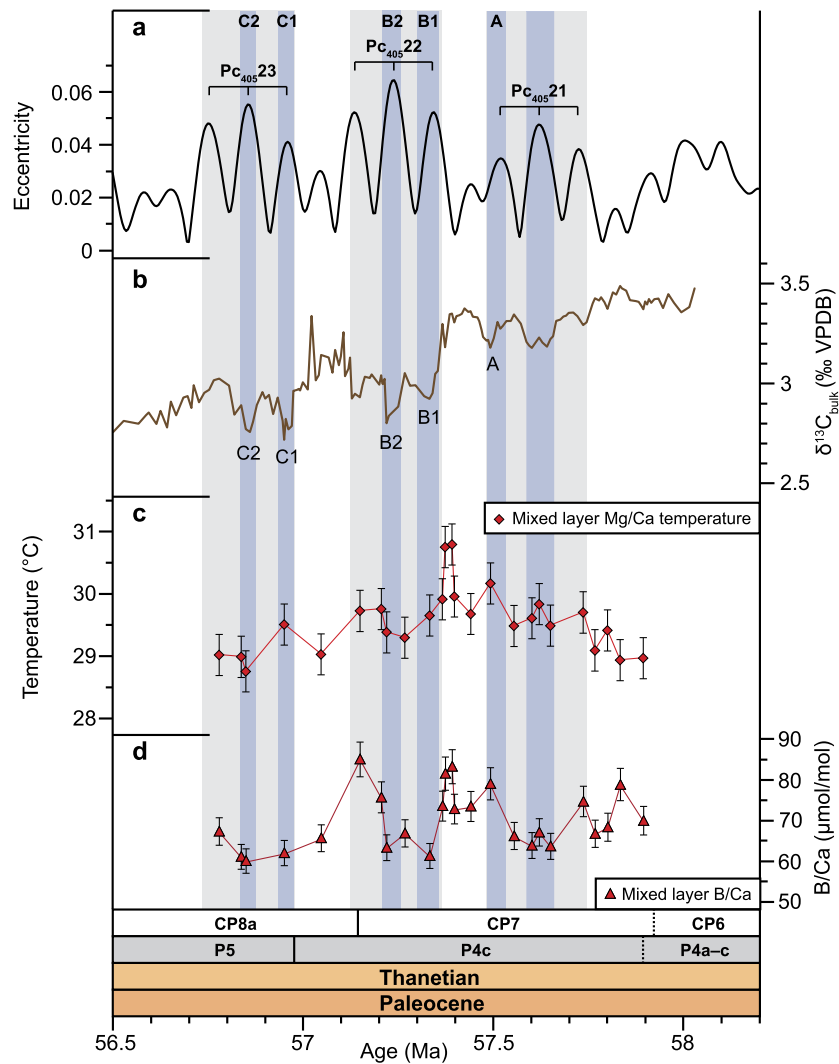


Fig. 8. Potential late Paleocene orbital cyclicality within the mixed layer Mg/Ca and B/Ca records. (a) La2010b orbital solution (Laskar et al., 2011). (b) IODP Hole U1443A/ODP Hole 758A $\delta^{13}\text{C}_{\text{bulk}}$ record, with latest Paleocene core gap indicated. PCIM = Paleocene Carbon Isotope Maximum. Carbon cycle events are named below the $\delta^{13}\text{C}_{\text{bulk}}$ curve. (c) Mixed layer Mg/Ca temperature record. (d) Mixed layer B/Ca record. Error bars indicate analytical uncertainty on the Mg/Ca and B/Ca measurements ($\pm 3\%$ and $\pm 5\%$, respectively). Pale grey intervals correspond to 405-kyr eccentricity maxima, while blue bars correspond to carbon cycle events associated with 100-kyr eccentricity maxima (named in panel b).

dian Ocean, consistent in magnitude and trend with the low latitude Pacific, suggesting comparable long-term thermal histories within these two major ocean basins during this time. We also observe an increase in $\delta^{18}\text{O}_{\text{sw}}$ of the mixed layer, suggesting an increase in net evaporation, and a collapse in the temperature gradient between mixed layer- and thermocline-dwelling foraminifera at ~ 57 Ma. The temperature gradient collapse could be explained by either the development of a more homogeneous water column with a thicker mixed layer and hence deeper thermocline, or depth migration of *Morozovella* in response to surface ocean warming. Synchronous warming within both the low latitudes and high latitude regions of deep water formation supports increasing atmospheric CO_2 concentrations as the primary driver of global climate during this time. The long-term decrease in mixed layer B/Ca also supports rising CO_2 levels within the ocean-atmosphere system and a decrease in pH and/or increase in DIC of the oceans. We observe a pacing consistent with 405-kyr eccentricity within the late Paleocene planktic B/Ca data, but not within the planktic Mg/Ca data, perhaps due to the magnitude of low latitude warming falling within analytical uncertainty.

Declaration of competing interest

The authors declare that they have no known competing financial interests or personal relationships that could have appeared to influence the work reported in this paper.

Acknowledgements

This work was principally funded by a European Consortium for Ocean Research Drilling (ECORD) Research Grant, the International Association of Sedimentologists (IAS) Postgraduate Research Grant Scheme, and the Natural Environment Research Council (NERC) Isotope Geosciences Facility (IP-1581-1115), awarded to James Barnet and Kate Littler. We also thank participants of the International Ocean Discovery Program Expedition 353 and Ocean Drilling Program Expedition 121 for collecting the sediment cores, as well as the Kochi Core Center for taking the requested samples on our behalf. LJJ acknowledges funding from the IODP-JRSO (NSF grant 1326927), KME acknowledges funding from NERC grants NE/H016457/1 and NE/P013112/1, and CVU acknowledges funding via NERC grant NE/N018508/1. Lastly, we thank two

anonymous reviewers for their comments which helped to improve the manuscript. The complete stable isotope and trace element datasets supporting this manuscript have been archived online in the PANGAEA database: <https://doi.pangaea.de/10.1594/PANGAEA.910789>.

Appendix A. Supplementary material

Supplementary material related to this article can be found online at <https://doi.org/10.1016/j.epsl.2020.116414>. These data include the Google map of the most important areas described in this article.

References

- Allen, K.A., Hönisch, B., Eggins, S.M., Yu, J., Spero, H.J., Elderfield, H., 2011. Controls on boron incorporation in cultured tests of the planktic foraminifer *Orbulina universa*. *Earth Planet. Sci. Lett.* 309, 291–301. <https://doi.org/10.1016/j.epsl.2011.07.010>.
- Allen, K.A., Hönisch, B., Eggins, S.M., Rosenthal, Y., 2012. Environmental controls on B/Ca in calcite tests of the tropical planktic foraminifer species *Globigerinoides ruber* and *Globigerinoides sacculifer*. *Earth Planet. Sci. Lett.* 351–352, 270–280. <https://doi.org/10.1016/j.epsl.2012.07.004>.
- Anand, P., Elderfield, H., Conte, M.H., 2003. Calibration of Mg/Ca thermometry in planktonic foraminifera from a sediment trap time series. *Paleoceanography* 18, 1050. <https://doi.org/10.1029/2002PA000846>.
- Babila, T.L., Rosenthal, Y., Wright, J.D., Miller, K.G., 2016. A continental shelf perspective of ocean acidification and temperature evolution during the Paleocene–Eocene Thermal Maximum. *Geology* 44, 275–278. <https://doi.org/10.1130/G37522.1>.
- Babila, T.L., Penman, D.E., Hönisch, B., Kelly, D.C., Bralower, T.J., Rosenthal, Y., Zachos, J.C., 2018. Capturing the global signature of surface ocean acidification during the Palaeocene–Eocene Thermal Maximum. *Philos. Trans. R. Soc. Lond. A* 376, 20170072. <https://doi.org/10.1098/rsta.2017.0072>.
- Barnet, J.S.K., Littler, K., Westerhold, T., Kroon, D., Leng, M.J., Bailey, I., Röhl, U., Zachos, J.C., 2019. A high-fidelity benthic stable isotope record of Late Cretaceous–Early Eocene climate change and carbon-cycling. *Paleoceanogr. Paleoclimatol.* 34, 672–691. <https://doi.org/10.1029/2019PA003556>.
- Bemis, B.E., Spero, H.J., Bijma, J., Lea, D.W., 1998. Reevaluation of the oxygen isotopic composition of planktonic foraminifera: experimental results and revised paleotemperature equations. *Paleoceanography* 13, 150–160. <https://doi.org/10.1029/98PA00070>.
- Boyle, E.A., Keigwin, L.D., 1985/86. Comparison of Atlantic and Pacific paleochemical records for the last 215,000 years: changes in deep ocean circulation and chemical inventories. *Earth Planet. Sci. Lett.* 76, 135–150. [https://doi.org/10.1016/0012-821X\(85\)90154-2](https://doi.org/10.1016/0012-821X(85)90154-2).
- Bralower, T.J., Zachos, J.C., Thomas, E., Parrow, M., Paull, C.K., Clay Kelly, D., Premoli Silva, I., Sliter, W.V., Lohmann, K.C., 1995. Late Paleocene to Eocene paleoceanography of the equatorial Pacific Ocean: stable isotopes recorded at Ocean Drilling Program Site 865, Allison Guyot. *Paleoceanography* 10, 841–865. <https://doi.org/10.1029/95PA01143>.
- Brown, R.E., Anderson, L.D., Thomas, E., Zachos, J.C., 2011. A core-top calibration of B/Ca in the benthic foraminifers *Nuttallides umbonifera* and *Oridorsalis umbonatus*: a proxy for Cenozoic bottom water carbonate saturation. *Earth Planet. Sci. Lett.* 310, 360–368. <https://doi.org/10.1016/j.epsl.2011.08.023>.
- Clemens, S.C., Kuhnt, W., LeVay, L.J., Anand, P., Ando, T., Bartol, M., et al., 2016. Site U1443. In: Clemens, S.C., Kuhnt, W., LeVay, L.J., the Expedition 353 Scientists (Eds.), *Proceedings of the International Ocean Discovery Program*, vol. 353. *International Ocean Discovery Program, College Station, Texas*, pp. 1–41.
- Cramwinckel, M.J., Huber, M., Kocken, I.J., Agnini, C., Bijl, P.K., Bohaty, S.M., Frieling, J., Goldner, A., Hilgen, F.J., Kip, E.L., Peterse, F., van der Ploeg, R., Röhl, U., Schouten, S., Sluijs, A., 2018. Synchronous tropical and polar temperature evolution in the Eocene. *Nature* 559, 382–386. <https://doi.org/10.1038/s41586-018-0272-2>.
- Dutton, A., Lohmann, K.C., Leckie, R.M., 2005. Insights from the Paleogene tropical Pacific: Foraminiferal stable isotope and elemental results from Site 1209, Shatsky Rise. *Paleoceanography* 20, PA3004. <https://doi.org/10.1029/2004PA001098>.
- Edgar, K.M., Anagnostou, E., Pearson, P.N., Foster, G.L., 2015. Assessing the impact of diagenesis on $\delta^{11}\text{B}$, $\delta^{13}\text{C}$, $\delta^{18}\text{O}$, Sr/Ca and B/Ca values in fossil planktic foraminiferal calcite. *Geochim. Cosmochim. Acta* 166, 189–209. <https://doi.org/10.1016/j.gca.2015.06.018>.
- Eley, Y.L., Thomson, W., Greene, S.E., Mandel, I., Edgar, K., Bendle, J.A., Dunkley Jones, T., 2019. OPTIMAL: a new machine learning approach for GDGT-based palaeothermometry. *Clim. Past Discuss.* <https://doi.org/10.5194/cp-2019-60>.
- Evans, D., Wade, B.S., Henehan, M., Erez, J., Müller, W., 2016a. Revisiting carbonate chemistry controls on planktic foraminifera Mg/Ca: implications for sea surface temperature and hydrology shifts over the Paleocene–Eocene Thermal Maximum and Eocene–Oligocene transition. *Clim. Past* 12, 819–835. <https://doi.org/10.5194/cp-12-819-2016>.
- Evans, D., Brierley, C., Raymo, M.R., Erez, J., Müller, W., 2016b. Planktic foraminifera shell chemistry response to seawater chemistry: Pliocene–Pleistocene seawater Mg/Ca, temperature and sea level change. *Earth Planet. Sci. Lett.* 438, 139–148. <https://doi.org/10.1016/j.epsl.2016.01.013>.
- Evans, D., Sagoo, N., Renema, W., Cotton, L., Müller, W., Todd, J.A., Saraswati, P.K., Stassen, P., Ziegler, M., Pearson, P.N., Valdes, P.J., Affek, H.P., 2018. Eocene greenhouse climate revealed by coupled clumped isotope–Mg/Ca thermometry. *Proc. Natl. Acad. Sci. USA* 115, 1174–1179. <https://doi.org/10.1073/pnas.1714744115>.
- Frieling, J., Gebhardt, H., Huber, M., Adekeye, O.A., Akande, S.O., Reichart, G.-J., Middelburg, J.J., Schouten, S., Sluijs, A., 2017. Extreme warmth and heat-stressed plankton in the tropics during the Paleocene–Eocene Thermal Maximum. *Sci. Adv.* 3, e1600891. <https://doi.org/10.1126/sciadv.1600891>.
- Gothmann, A.M., Stolarski, J., Adkins, J.F., Schoene, B., Dennis, K.J., Schrag, D.P., Mazur, M., Bender, M.L., 2015. Fossil corals as an archive of secular variations in seawater chemistry since the Mesozoic. *Geochim. Cosmochim. Acta* 160, 188–208. <https://doi.org/10.1016/j.gca.2015.03.018>.
- Gray, W.R., Weldeab, S., Lea, D.W., Rosenthal, Y., Gruber, N., Donner, B., Fischer, G., 2018. The effects of temperature, salinity, and the carbonate system on Mg/Ca in *Globigerinoides ruber* (white): a global sediment trap calibration. *Earth Planet. Sci. Lett.* 482, 607–620. <https://doi.org/10.1016/j.epsl.2017.11.026>.
- Greene, S.E., Ridgwell, A., Kirtland Turner, S., Schmidt, D.N., Pälike, H., Thomas, E., Greene, L.K., Hoogakker, B.A.A., 2019. Early Cenozoic decoupling of climate and carbonate compensation depth trends. *Paleoceanogr. Paleoclimatol.* 34, 930–945. <https://doi.org/10.1029/2019PA003601>.
- Hague, A.M., Thomas, D.J., Huber, M., Korty, R., Woodard, S.C., Blake Jones, L., 2012. Convection of North Pacific deep water during the early Cenozoic. *Geology* 40, 527–530. <https://doi.org/10.1130/G32886.1>.
- Harper, D.T., Zeebe, R., Hönisch, B., Schrader, C.D., Lourens, L.J., Zachos, J.C., 2018. Subtropical sea-surface warming and increased salinity during Eocene Thermal Maximum 2. *Geology* 46, 187–190. <https://doi.org/10.1130/G39658.1>.
- Hay, W.W., DeConto, R., Wold, C.N., Wilson, K.M., Voigt, S., Schulz, M., Wold-Rosssby, A., Dullo, W.-C., Ronov, A.B., Balukhovskiy, A.N., Soeding, E., 1999. *Alternative Global Cretaceous paleogeography*. In: Barrera, E., Johnson, C. (Eds.), *The Evolution of Cretaceous Ocean/Climate Systems*. In: *Special Papers – Geological Society of America*, vol. 332, pp. 1–47.
- Haynes, L.L., Hönisch, B., Holland, K., Rosenthal, Y., Eggins, S.M., 2019. Evaluating the planktic foraminiferal B/Ca proxy for application to deep time paleoceanography. *Earth Planet. Sci. Lett.* 528, 115824. <https://doi.org/10.1016/j.epsl.2019.11.5824>.
- Hollis, C.J., Taylor, K.W.R., Handley, L., Pancost, R.D., Huber, M., Creech, J.B., Hines, B.R., Crouch, E.M., Morgans, H.E.G., Crampton, J.S., Gibbs, S., Pearson, P.N., Zachos, J.C., 2012. Early Paleogene temperature history of the Southwest Pacific Ocean: reconciling proxies and models. *Earth Planet. Sci. Lett.* 349–350, 53–66. <https://doi.org/10.1016/j.epsl.2012.06.024>.
- Hollis, C.J., Dunkley Jones, T., Anagnostou, E., Bijl, P.K., Cramwinckel, M.J., Cui, Y., Dickens, G.R., Edgar, K.M., Eley, Y., Evans, D., Foster, G.L., Frieling, J., Inglis, G.N., Kennedy, E.M., Kozdon, R., Laurentano, V., Lear, C.H., Littler, K., Meckler, N., Naafs, B.D.A., Pälike, H., Pancost, R.D., Pearson, P., Royer, D.L., Salzmann, U., Schubert, B., Seebeck, H., Sluijs, A., Speijer, R., Stassen, P., Tierney, J., Tripati, A., Wade, B., Westerhold, T., Witkowski, C., Zachos, J.C., Zhang, Y.G., Huber, M., Lunt, D.J., 2019. The DeepMIP contribution to PMIP4: methodologies for selection, compilation and analysis of latest Paleocene and early Eocene climate proxy data, incorporating version 0.1 of the DeepMIP database. *Geosci. Model Dev. Discuss.*, 1–98. <https://doi.org/10.5194/gmd-2018-309>.
- John, E.H., Wilson, J.D., Pearson, P.N., Ridgwell, A., 2014. Temperature-dependent remineralization and carbon cycling in the warm Eocene oceans. *Palaeogeogr. Palaeoclimatol. Palaeoecol.* 413, 158–166. <https://doi.org/10.1016/j.palaeo.2014.05.019>.
- Kim, J.-H., van der Meer, J., Schouten, S., Helmke, P., Willmott, V., Sangiorgi, F., Koç, N., Hopmans, E.C., Sinnighe Damsté, J.S., 2010. New indices and calibrations derived from the distribution of crenarchaeal isoprenoid tetraether lipids: implications for past sea surface temperature reconstructions. *Geochim. Cosmochim. Acta* 74, 4639–4654. <https://doi.org/10.1016/j.gca.2010.05.027>.
- Komar, N., Zeebe, R.E., Dickens, G.R., 2013. Understanding long-term carbon cycle trends: the late Paleocene through the early Eocene. *Paleoceanography* 28, 650–662. <https://doi.org/10.1002/palo.20060>.
- Kozdon, R., Kelly, D.C., Kitajima, K., Strickland, A., Fournelle, J.H., Valley, J.W., 2013. In situ $\delta^{18}\text{O}$ and Mg/Ca analyses of diagenetic and planktic foraminiferal calcite preserved in a deep-sea record of the Paleocene–Eocene thermal maximum. *Paleoceanography* 28, 517–528. <https://doi.org/10.1002/palo.20048>.
- Laskar, J., Fienga, A., Gastineau, M., Manche, H., 2011. La2010: a new orbital solution for the long-term motion of the Earth. *Astron. Astrophys.* 532, A89. <https://doi.org/10.1051/0004-6361/201116836>.
- Laurentano, V., Littler, K., Polling, M., Zachos, J.C., Lourens, L.J., 2015. Frequency, magnitude and character of hyperthermal events at the onset of the Early Eocene Climatic Optimum. *Clim. Past* 11, 1313–1324. <https://doi.org/10.5194/cp-11-1313-2015>.

- Lear, C.H., Elderfield, H., Wilson, P.A., 2000. Cenozoic deep-sea temperatures and global ice volumes from Mg/Ca in benthic foraminiferal calcite. *Science* 287, 269–272. <https://doi.org/10.1126/science.287.5451.269>.
- Lear, C.H., Coxall, H.K., Foster, G.L., Lunt, D.J., Mawbey, E.M., Rosenthal, Y., Sosdian, S.M., Thomas, E., Wilson, P.A., 2015. Neogene ice volume and ocean temperatures: insights from infaunal foraminiferal Mg/Ca paleothermometry. *Paleoceanography* 30, 1437–1454. <https://doi.org/10.1002/2015PA002833>.
- Lemarchand, D., Gaillardet, J., Lewin, É., Allègre, C.J., 2002. Boron isotope systematics in large rivers: implications for the marine boron budget and paleo-pH reconstruction over the Cenozoic. *Chem. Geol.* 190, 123–140. [https://doi.org/10.1016/S0009-2541\(02\)00114-6](https://doi.org/10.1016/S0009-2541(02)00114-6).
- Littler, K., Röhl, U., Westerhold, T., Zachos, J.C., 2014. A high-resolution benthic stable-isotope record for the South Atlantic: implications for orbital-scale changes in Late Paleocene–Early Eocene climate and carbon cycling. *Earth Planet. Sci. Lett.* 401, 18–30. <https://doi.org/10.1016/j.epsl.2014.05.054>.
- Locarnini, R.A., Mishonov, A.V., Antonov, J.I., Boyer, T.P., Garcia, H.E., Baranova, O.K., Zweng, M.M., Paver, C.R., Reagan, J.R., Johnson, D.R., Hamilton, M., Seidov, D., 2013. *World Ocean Atlas 2013, Volume 1: Temperature*. In: Levitus, S., Mishonov, A. (Eds.), NOAA Atlas NESDIS 73, 40 p.
- Makarova, M., Wright, J.D., Miller, K.G., Babila, T.L., Rosenthal, Y., Park, J.I., 2017. Hydrographic and ecologic implications of foraminiferal stable isotopic response across the U.S. mid-Atlantic continental shelf during the Paleocene–Eocene Thermal Maximum. *Paleoceanography* 32, PA002985. <https://doi.org/10.1002/2016PA002985>.
- Matsui, H., Nishi, H., Takashima, R., Kuroyanagi, A., Ikehara, M., Takayanagi, H., Iryu, Y., 2016. Changes in the depth habitat of the Oligocene planktic foraminifera (*Dentoglobigerina venezuelana*) induced by thermocline deepening in the eastern equatorial Pacific. *Paleoceanogr. Paleoclimatol.* 31, 715–731. <https://doi.org/10.1002/2016PA002950>.
- McInerney, F.A., Wing, S.L., 2011. The Paleocene–Eocene Thermal Maximum: a perturbation of carbon cycle, climate, and biosphere with implications for the future. *Annu. Rev. Earth Planet. Sci.* 39, 489–516. <https://doi.org/10.1146/annurev-earth-040610-133431>.
- Nunes, F., Norris, R.D., 2006. Abrupt reversal in ocean overturning during the Paleocene/Eocene warm period. *Nature* 439, 60–63. <https://doi.org/10.1038/nature04386>.
- Pearson, P.N., Olsson, R.K., Huber, B.T., Hemleben, C., Berggren, W.A., Coxall, H.K., 2006. Chapter 1: overview of Eocene planktonic foraminiferal taxonomy, paleoecology, phylogeny, and biostratigraphy. In: Pearson, P.N., Olsson, R.K., Huber, B.T., Hemleben, C., Berggren, W.A. (Eds.), *Atlas of Eocene Planktonic Foraminifera*. In: Cushman Foundation Special Publication, vol. 41, pp. 11–28.
- Pearson, P.N., Wade, B.S., 2009. Taxonomy and stable isotope paleoecology of well-preserved planktonic foraminifera from the uppermost Oligocene of Trinidad. *J. Foraminiferal Res.* 39, 191–217. <https://doi.org/10.2113/gsjfr.39.3.191>.
- Penman, D.E., Hönisch, B., Zeebe, R.E., Thomas, E., Zachos, J.C., 2014. Rapid and sustained surface ocean acidification during the Paleocene–Eocene Thermal Maximum. *Paleoceanography* 29, 357–369. <https://doi.org/10.1002/2014PA002621>.
- Sagoo, N., Valdes, P., Flecker, R., Gregoire, L.J., 2013. The Early Eocene equable climate problem: can perturbations of climate model parameters identify possible solutions? *Philos. Trans. R. Soc. Lond. A* 371, 1–35. <https://doi.org/10.1098/rsta.2013.0123>.
- Shackleton, N.J., Kennett, J.P., 1975. Paleotemperature history of the Cenozoic and the initiation of Antarctic glaciation: oxygen and carbon isotope analyses in DSDP sites 277, 279 and 281. In: Kennett, J.P., et al. (Eds.), *Initial Reports of the Deep Sea Drilling Project 29*. U.S. Govt. Printing Office, Washington.
- Shipboard Scientific Party, 1989. Site 758. In: Peirce, J., Weissel, J., et al. (Eds.), *Proceedings of the Ocean Drilling Program, Initial Reports 121*. Ocean Drilling Program, College Station, Texas, pp. 359–453.
- Si, W., Aubry, M.-P., 2018. Vital effects and ecologic adaptation of photosymbiont-bearing planktonic foraminifera during the Paleocene–Eocene Thermal Maximum, implications for paleoclimate. *Paleoceanogr. Paleoclimatol.* 33, 112–125. <https://doi.org/10.1002/2017PA003219>.
- Slotnick, B.S., Lauretano, V., Backman, J., Dickens, G.R., Sluijs, A., Lourens, L., 2015. Early Paleogene variations in the calcite compensation depth: new constraints using old borehole sediments from across Ninetyeast Ridge, central Indian Ocean. *Clim. Past* 11, 473–493. <https://doi.org/10.5194/cp-11-473-2015>.
- Stainbank, S., Kroon, D., Rüggeberg, A., Raddatz, J., de Leau, E.S., Zhang, M., Spezzaferri, S., 2019. Controls on planktonic foraminifera apparent calcification depths for the northern equatorial Indian Ocean. *PLoS ONE* 14, e0222299. <https://doi.org/10.1371/journal.pone.0222299>.
- Stott, L.D., Kennett, J.P., Shackleton, N.J., Corfield, R.M., 1990. The evolution of Antarctic surface waters during the Paleogene: inferences from the stable isotopic compositions of planktonic foraminifera, ODP Leg 113. In: Barker, P.F., Kennett, J.P., et al. (Eds.), *Proceedings of the Ocean Drilling Program, Scientific Results, vol. 113*, pp. 849–863.
- Torsvik, T.H., Van der Voo, R., Preeden, U., Niocail, C. Mac, Steinberger, B., Doubrovine, P.V., van Hinsbergen, D.J.J., Domeier, M., Gaina, C., Tohver, E., Meert, J.G., McCausland, P.J.A., Cocks, L.R.M., 2012. Phanerozoic polar wander, palaeogeography and dynamics. *Earth-Sci. Rev.* 114, 325–368. <https://doi.org/10.1016/j.earscirev.2012.06.007>.
- Thomas, D.J., 2004. Evidence for deep-water production in the North Pacific Ocean during the early Cenozoic warm interval. *Nature* 430, 65–68. <https://doi.org/10.1038/nature02639>.
- Thomas, D.J., Lyle, M., Moore Jr., T.C., Rea, D.K., 2008. Paleogene deepwater mass composition of the tropical Pacific and implications for thermohaline circulation in a greenhouse world. *Geochem. Geophys. Geosyst.* 9, Q02002. <https://doi.org/10.1029/2007GC001748>.
- Tripathi, A.K., Delaney, M.L., Zachos, J.C., Anderson, L.D., Kelly, D.C., Elderfield, H., 2003. Tropical sea-surface temperature reconstruction for the early Paleogene using Mg/Ca ratios of planktonic foraminifera. *Paleoceanography* 18, 1101. <https://doi.org/10.1029/2003PA000937>.
- Tripathi, A.K., Elderfield, H., 2004. Abrupt hydrographic changes in the equatorial Pacific and subtropical Atlantic from foraminiferal Mg/Ca indicate greenhouse origin for the thermal maximum at the Paleocene–Eocene boundary. *Geochem. Geophys. Geosyst.* 5, 1–11. <https://doi.org/10.1029/2003GC000631>.
- Van Hinsbergen, D.J.J., De Groot, L.V., Van Schaik, S.J., Spakman, W., Bijl, P.K., Sluijs, A., Langereis, C.G., Brinkhuis, H., 2015. A paleolatitude calculator for paleoclimate studies. *PLoS ONE* 10, 1–21. <https://doi.org/10.1371/journal.pone.0126946>.
- Westerhold, T., Röhl, U., Donner, B., Zachos, J.C., 2018. Global extent of early Eocene hyperthermal events: a new Pacific benthic foraminiferal isotope record from Shatsky Rise (ODP Site 1209). *Paleoceanogr. Paleoclimatol.* 33, 626–642. <https://doi.org/10.1029/2017PA003306>.
- Wilkinson, C.M., Ganerød, M., Hendriks, B.W.H., Eide, E.A., 2016. Compilation and appraisal of geochronological data from the North Atlantic Igneous Province (NAIP). In: Péron-Pinvidic, G., Hopper, J.R., Stoker, M.S., Gaina, C., Doornbeek, J.C., Funck, T., Arting, U.E. (Eds.), *The NE Atlantic Region: A Reappraisal of Crustal Structure, Tectonostratigraphy and Magmatic Evolution*. *Geol. Soc. (Lond.) Spec. Publ.* 447, 69–103.
- Zachos, J.C., Rea, D.K., Seto, K., Nomura, R., Niitsuma, N., 1992. Paleogene and Early Neogene deep water paleoceanography of the Indian Ocean as determined from benthic foraminiferal stable carbon and oxygen isotope records. In: *Synthesis of Results from Scientific Drilling in the Indian Ocean*. In: *Geophysical Monographs*, vol. 70, pp. 351–385.
- Zachos, J.C., Stott, L.D., Lohmann, K.C., 1994. Evolution of early Cenozoic marine temperatures. *Paleoceanography* 9, 353–387. <https://doi.org/10.1029/93PA03266>.
- Zachos, J.C., Wara, M.W., Bohaty, S., Delaney, M.L., Petrizzo, M.R., Brill, A., Bralower, T.J., Premoli-Silva, I., 2003. A transient rise in tropical sea surface temperature during the Paleocene–Eocene Thermal Maximum. *Science* 302, 1551–1554. <https://doi.org/10.1126/science.1090110>.
- Zachos, J.C., Röhl, U., Schellenberg, S.A., Sluijs, A., Hodell, D.A., Kelly, D.C., Thomas, E., Nicolo, M., Raffi, I., Lourens, L.J., McCarren, H., Kroon, D., 2005. Rapid acidification of the ocean during the Paleocene–Eocene Thermal Maximum. *Science* 308, 1611–1615. <https://doi.org/10.1126/science.1109004>.
- Zachos, J.C., McCarren, H., Murphy, B., Röhl, U., Westerhold, T., 2010. Tempo and scale of late Paleocene and early Eocene carbon isotope cycles: implications for the origin of hyperthermals. *Earth Planet. Sci. Lett.* 299, 242–249. <https://doi.org/10.1016/j.epsl.2010.09.004>.
- Zeebe, R.E., Tyrrell, T., 2019. History of carbonate ion concentration over the last 100 million years II: revised calculations and new data. *Geochim. Cosmochim. Acta* 257, 373–392. <https://doi.org/10.1016/j.gca.2019.02.041>.